

***Stxbp1/Munc18-1* haploinsufficiency impairs inhibition and mediates key neurological features of *STXBPI* encephalopathy**

Wu Chen^{1,2}, Zhao-Lin Cai^{1,2}, Eugene S. Chao^{1,2}, Hongmei Chen^{1,2}, Colleen M. Longley^{2,3},
Shuang Hao^{4,5}, Hsiao-Tuan Chao^{1,4,5,6,7}, Joo Hyun Kim^{1,2}, Jessica E. Messier^{1,2}, Huda Y.
Zoghbi^{1,3,4,5,6,8}, Jianrong Tang^{4,5}, John W. Swann^{1,2,4}, Mingshan Xue^{1,2,3,6,*}

¹Department of Neuroscience, Baylor College of Medicine, Houston, Texas 77030, USA

²The Cain Foundation Laboratories, Jan and Dan Duncan Neurological Research Institute at
Texas Children's Hospital, Houston, Texas 77030, USA

³Program in Developmental Biology, Baylor College of Medicine, Houston, Texas 77030, USA

⁴Department of Pediatrics, Division of Neurology and Developmental Neuroscience, Baylor
College of Medicine, Houston, Texas 77030, USA

⁵Jan and Dan Duncan Neurological Research Institute at Texas Children's Hospital, Houston,
Texas 77030, USA

⁶Department of Molecular and Human Genetics, Baylor College of Medicine, Houston, Texas
77030, USA

⁷McNair Medical Institute, The Robert and Janice McNair Foundation, Houston, Texas 77030,
USA

⁸Howard Hughes Medical Institute, Baylor College of Medicine, Houston, Texas 77030, USA

*Correspondence: mxue@bcm.edu

Abstract (150 words)

Mutations in genes encoding synaptic proteins cause many neurodevelopmental disorders, with the majority affecting postsynaptic apparatuses and much fewer in presynaptic proteins. Syntaxin-binding protein 1 (STXBP1, also known as MUNC18-1) is an essential component of the presynaptic neurotransmitter release machinery. *De novo* heterozygous pathogenic variants in *STXBP1* are among the most frequent causes of neurodevelopmental disorders including intellectual disabilities and epilepsies. These disorders, collectively referred to as *STXBP1* encephalopathy, encompass a broad spectrum of neurologic and psychiatric features, but the pathogenesis remains elusive. Here we modeled *STXBP1* encephalopathy in mice and found that *Stxbp1* haploinsufficiency caused cognitive, psychiatric, and motor dysfunctions, as well as cortical hyperexcitability and seizures. Furthermore, *Stxbp1* haploinsufficiency reduced cortical inhibitory neurotransmission via distinct mechanisms from parvalbumin-expressing and somatostatin-expressing interneurons. These results demonstrate that *Stxbp1* haploinsufficient mice recapitulate cardinal features of *STXBP1* encephalopathy and indicate that GABAergic synaptic dysfunction is likely a crucial contributor to disease pathogenesis.

Introduction

Human genetic studies of neurodevelopmental disorders continue to uncover pathogenic variants in genes encoding synaptic proteins (Hoischen et al., 2014; Zhu et al., 2014; Deciphering Developmental Disorders Study, 2015; 2017; Stessman et al., 2017; Lindy et al., 2018), demonstrating the importance of these proteins for neurologic and psychiatric features. The molecular and cellular functions of many of these synaptic proteins have been extensively studied. However, to understand the pathological mechanisms underlying these synaptic

disorders, in-depth neurological and behavioral studies in animal models are necessary. While it is difficult to perform such studies for all disorders, this knowledge gap can be significantly narrowed by studying a few prioritized genes that are highly penetrant and affect a broad spectrum of neurologic and psychiatric features common among neurodevelopmental disorders (Hoischen et al., 2014; Ogden et al., 2016). Syntaxin-binding protein 1 (STXBP1, also known as MUNC18-1) is one such example because its molecular and cellular functions are well understood (Rizo and Xu, 2015), its pathogenic variants are emerging as prevalent causes of multiple neurodevelopmental disorders (Stamberger et al., 2016), and yet it remains unclear how its dysfunction causes disease.

Stxbp1/Munc18-1 is involved in synaptic vesicle docking, priming, and fusion through multiple interactions with the neuronal soluble *N*-ethylmaleimide-sensitive factor-attachment protein receptors (SNAREs) (Rizo and Xu, 2015). Genetic deletion of Stxbp1 in worms, flies, mice, and fish abolishes neurotransmitter release and leads to lethality and cell-intrinsic degeneration of neurons (Harrison et al., 1994; Verhage et al., 2000; Weimer et al., 2003; Heeroma et al., 2004; Grone et al., 2016). In humans, *STXBP1 de novo* heterozygous mutations cause several of the most severe forms of epileptic encephalopathies including Ohtahara syndrome (Saitsu et al., 2008; 2010), West syndrome (Deprez et al., 2010; Otsuka et al., 2010), Lennox-Gastaut syndrome (Carvill et al., 2013; Epi4K Consortium et al., 2013), Dravet syndrome (Carvill et al., 2014), and other types of early-onset epileptic encephalopathies (Deprez et al., 2010; Mignot et al., 2011; Stamberger et al., 2016). Furthermore, *STXBP1* is one of the most frequently mutated genes in sporadic intellectual disabilities and developmental disorders (Hamdan et al., 2009; 2011; Rauch et al., 2012; Deciphering Developmental Disorders Study, 2015; 2017; Suri et al.,

2017). All *STXBPI* encephalopathy patients show intellectual disability, mostly severe to profound, and 95% of patients have epilepsy (Stamberger et al., 2016). More than 90% of patients have motor deficits, such as dystonia, spasticity, ataxia, hypotonia and tremor. Other clinical features in subsets of patients include developmental delay, hyperactivity, anxiety, stereotypies, aggressive behaviors, and autistic features (Hamdan et al., 2009; Deprez et al., 2010; Mignot et al., 2011; Milh et al., 2011; Campbell et al., 2012; Rauch et al., 2012; Weckhuysen et al., 2013; Boutry-Kryza et al., 2015; Stamberger et al., 2016; Suri et al., 2017).

STXBPI encephalopathy is mostly caused by haploinsufficiency because more than 60% of the reported mutations are either deletions, nonsense, frameshift, or splice site variants (Stamberger et al., 2016). A subset of missense variants were shown to destabilize the protein (Saitou et al., 2008; 2010; Guiberson et al., 2018; Kovačević et al., 2018) and cause aggregation to further reduce the wild type (WT) protein levels (Guiberson et al., 2018). Thus, partial loss-of-function of *Stxbp1* *in vivo* would offer opportunities to model *STXBPI* encephalopathy and study its pathogenesis. Indeed, removing *stxbp1b*, one of the two *STXBPI* homologs in zebrafish, caused spontaneous electrographic seizures (Grone et al., 2016). Three different *Stxbp1* null alleles have been generated in mice (Verhage et al., 2000; Miyamoto et al., 2017; Kovačević et al., 2018). However, previous characterization of the corresponding heterozygous knockout mice was limited in scope, used relatively small cohorts, and yielded inconsistent results. For example, the reported cognitive phenotypes in mutant mice are mild or inconsistent between studies (Miyamoto et al., 2017; Kovačević et al., 2018; Orock et al., 2018). Motor dysfunctions and several psychiatric deficits were not reported in previous studies (Hager et al., 2014; Miyamoto et al., 2017; Kovačević et al., 2018; Orock et al., 2018). Thus, a comprehensive neurological and

behavioral study of *Stxbp1* haploinsufficiency models is still lacking. Interestingly, *Stxbp1* protein levels were reduced by only 25% in the brain of one line of previous *Stxbp1* heterozygous knockout mice (Orock et al., 2018) and 25% in the cortex and 50% in the hippocampus of another line (Miyamoto et al., 2017). Although *STXBP1* levels in human patients are unknown, mouse models with a stronger reduction in *Stxbp1* levels are desirable to determine to what extent *Stxbp1* haploinsufficient mice can recapitulate the neurological phenotypes of *STXBP1* encephalopathy. Furthermore, it remains elusive how *STXBP1* haploinsufficiency *in vivo* leads to hyperexcitable neural circuits and neurological deficits.

To address these questions and enhance the robustness and reproducibility of preclinical models of *STXBP1* haploinsufficiency, we developed two new genetically distinct *Stxbp1* haploinsufficiency mouse models and performed parallel studies on both of them. These mutant mice showed a 50% reduction of *Stxbp1* protein levels in most brain regions and recapitulated all key phenotypes observed in the human condition including seizures and impairments in cognitive, psychiatric, and motor functions. Electrophysiological and optogenetic experiments revealed that *Stxbp1* haploinsufficiency reduced cortical inhibition through two distinct mechanisms from two main classes of GABAergic neurons: reducing the synaptic strength of parvalbumin-expressing (Pv) interneurons and decreasing the connectivity of somatostatin-expressing (Sst) interneurons. Thus, these results demonstrate a crucial role of *Stxbp1* in neurologic and psychiatric functions and indicate that *Stxbp1* haploinsufficient mice are construct- and face-valid models of *STXBP1* encephalopathy. Furthermore, the reduced inhibition is likely a major contributor to the cortical hyperexcitability and neurobehavioral phenotypes. The differential effects on Pv and Sst interneuron-mediated inhibition suggest

synapse-specific functions of *Stxbp1* and also highlight the necessity of studying synaptic specificity and diversity in neural circuits of synaptopathies.

Results

Generation of two new genetically distinct *Stxbp1* haploinsufficiency mouse models

To model *STXBPI* haploinsufficiency in mice, we first generated a knockout-first (KO-first) allele (*tm1a*), in which the *Stxbp1* genomic locus was targeted with a multipurpose cassette (Testa et al., 2004; Skarnes et al., 2011). The targeted allele contains a splice acceptor site from *Engrailed 2* (*En2SA*), an encephalomyocarditis virus internal ribosomal entry site (*IRES*), *lacZ*, and SV40 polyadenylation element (pA) that trap the transcripts after exon 6, thereby truncating the *Stxbp1* mRNA. The trapping cassette (*En2SA-IRES-lacZ-pA*) and exon 7 are flanked by two *FRT* sites and two *loxP* sites, respectively (**Figure 1-supplement 1A**). By sequentially crossing with Flp and Cre germline deleter mice, we removed both the trapping cassette and exon 7 from the heterozygous KO-first mice, which leads to a premature stop codon in exon 8 and generates a conventional knockout (KO) allele (*tm1d*) (**Figure 1A**). Heterozygous KO (*Stxbp1^{tm1d/+}*) and KO-first (*Stxbp1^{tm1a/+}*) mice are maintained on the C57BL/6J isogenic background for all experiments.

Homozygous mutants (*Stxbp1^{tm1d/tm1d}* and *Stxbp1^{tm1a/tm1a}*) died immediately after birth because they were completely paralyzed and could not breathe, consistent with the previous *Stxbp1* null alleles (Verhage et al., 2000; Miyamoto et al., 2017). Western blots with antibodies recognizing either the N- or C-terminus of *Stxbp1* showed that at embryonic day 17.5, *Stxbp1* protein was absent in *Stxbp1^{tm1d/tm1d}* and *Stxbp1^{tm1a/tm1a}* mice, and reduced by 50% in *Stxbp1^{tm1d/+}* and

Stxbp1^{tm1a/+} mice (**Figure 1-supplement 1B,C**), indicating that both alleles are null alleles. We surveyed the *Stxbp1* protein levels in different brain regions of *Stxbp1*^{tm1d/+} and *Stxbp1*^{tm1a/+} mice at 3 months of age. *Stxbp1* was reduced by 40–50% in most brain areas except the cerebellum and olfactory bulb where the reduction was 20–30% (**Figure 1B,C**). These results demonstrate that *Stxbp1*^{tm1d/+} and *Stxbp1*^{tm1a/+} are indeed *Stxbp1* haploinsufficient mice. In theory, the KO and KO-first alleles could produce a truncated *Stxbp1* protein of 18 kD and 16 kD, respectively. However, no such truncated proteins were observed in either heterozygous or homozygous mutants (**Figure 1-supplement 1B**), most likely because the truncated *Stxbp1* transcripts were degraded due to nonsense-mediated mRNA decay (Chang et al., 2007).

***Stxbp1* haploinsufficient mice show a reduction in survival and body weights, and developed hindlimb clasp**

We bred *Stxbp1*^{tm1d/+} and *Stxbp1*^{tm1a/+} mice with WT mice and found that at the time of genotyping (i.e., around postnatal week 3) *Stxbp1*^{tm1d/+} and *Stxbp1*^{tm1a/+} mice are 40% and 43% of the total offspring, respectively (**Figure 1D** and **Figure 1-supplement 2A**), indicating a postnatal lethality phenotype. However, the lifespans of many mutant mice that survived through weaning were similar to those of WT littermates (**Figure 1-supplement 2B**). Thus, *Stxbp1* haploinsufficient mice show reduced survival, but this phenotype is not fully penetrant. *Stxbp1*^{tm1d/+} and *Stxbp1*^{tm1a/+} mice appeared smaller and their body weights were consistently about 20% less than their sex- and age-matched WT littermates (**Figure 1E,F**). At 4 weeks of age, *Stxbp1*^{tm1d/+} and *Stxbp1*^{tm1a/+} mice began to exhibit abnormal hindlimb clasp, indicative of dystonia or spasticity (**Figure 1E**). By the age of 3 months, almost all mutant mice developed hindlimb clasp (**Figure 1G**). Thus, these observations indicate neurological deficits in *Stxbp1*

haploinsufficient mice.

Guided by the symptoms of *STXBP1* encephalopathy human patients, we sought to perform behavioral and physiological assays to further examine the neurologic and psychiatric functions in male and female *Stxbp1* haploinsufficient mice and their sex- and age-matched WT littermates.

Impaired motor and normal sensory functions in *Stxbp1* haploinsufficient mice

Motor impairments including dystonia, spasticity, ataxia, hypotonia, and tremor are frequently observed in *STXBP1* encephalopathy patients. Thus, we first assessed general locomotion by the open-field test where a mouse is allowed to freely explore an arena (**Figure 2A**). The locomotion of *Stxbp1*^{tm1d/+} and *Stxbp1*^{tm1a/+} mice was largely normal, but they traveled longer distances and faster than WT mice, indicating that *Stxbp1* haploinsufficient mice are hyperactive (**Figure 2B,C**). Both *Stxbp1*^{tm1d/+} and *Stxbp1*^{tm1a/+} mice explored the center region of the arena less than WT mice (**Figure 2D**) and made less vertical movements (**Figure 2E**), indicating that the mutant mice are more anxious. This anxiety phenotype was later confirmed by two other assays that specifically assess anxiety (see below). We used a variety of assays to further evaluate motor functions. *Stxbp1* haploinsufficient mice performed similarly to WT mice in the rotarod test, dowel test, inverted screen test, and wire hang test (**Figure 2-supplement 1**). However, the forelimb grip strength of *Stxbp1* haploinsufficient mice was weaker (**Figure 2F**). Furthermore, in the foot slip test where a mouse is allowed to walk on a wire grid, both *Stxbp1*^{tm1d/+} and *Stxbp1*^{tm1a/+} mice were not able to place their paws precisely on the wire to hold themselves and made many more foot slips than WT mice (**Figure 2G**). To assess the agility of mice, we performed the vertical pole test, which is often used to measure the bradykinesia of parkinsonism.

When mice were placed head-up on the top of a vertical pole, it took mutant mice much longer to orient themselves downward and descend the pole than WT mice (**Figure 2H**). Together, these results indicate that *Stxbp1* haploinsufficient mice do not develop ataxia, but their fine motor coordination and muscle strength are reduced.

We next examined the acoustic sensory function and found that *Stxbp1*^{tm1d/+} and *Stxbp1*^{tm1a/+} mice showed normal startle responses to different levels of sound (**Figure 2-supplement 2A**). To test sensorimotor gating, we measured the pre-pulse inhibition where the startle response to a strong sound is reduced by a preceding weaker sound. *Stxbp1*^{tm1d/+} and *Stxbp1*^{tm1a/+} mice displayed similar pre-pulse inhibition as WT mice (**Figure 2-supplement 2B**). They also had normal nociception as measured by the hot plate test (**Figure 2-supplement 2C**). Thus, the sensory functions and sensorimotor gating of *Stxbp1* haploinsufficient mice are normal.

Cognitive functions of *Stxbp1* haploinsufficient mice are severely impaired

Intellectual disability is a core feature of *STXBP1* encephalopathy, as the vast majority of patients have severe to profound intellectual disability (Stamberger et al., 2016). However, the learning and memory deficits described in the previous *Stxbp1* heterozygous knockout mice are mild and inconsistent (Miyamoto et al., 2017; Kovačević et al., 2018; Orock et al., 2018). To assess cognitive functions, we tested *Stxbp1* haploinsufficient mice in three different paradigms, object recognition, associative learning and memory, and working memory. First, we performed the novel object recognition test that exploits the natural tendency of mice to explore novel objects to evaluate their memories. This task is thought to depend on the hippocampus and cortex (Antunes and Biala, 2012; Cohen and Stackman, 2015). When tested with an inter-trial interval

of 24 hours, WT mice interacted more with the novel object than the familiar object, whereas *Stxbp1*^{tm1d/+} and *Stxbp1*^{tm1a/+} mice interacted equally between the familiar and novel objects (**Figure 3A**). We also evaluated *Stxbp1*^{tm1d/+} mice with an inter-trial interval of 5 minutes and observed a similar deficit (**Figure 3-supplement 1A**). We noticed that mutant mice overall spent less time interacting with the objects than WT mice during the trials (**Figure 3-supplement 1B**), which might reduce their “memory load” of the objects. We hence allowed *Stxbp1*^{tm1d/+} mice to spend twice as much time as WT mice in each trial to increase their interaction time with the objects (**Figure 3-supplement 1C**), but they still showed a similar deficit in recognition memory (**Figure 3-supplement 1D**). Thus, both long-term and short-term recognition memories are impaired in *Stxbp1* haploinsufficient mice.

Second, we used the Pavlovian fear conditioning paradigm to evaluate associative learning and memory, in which a mouse learns to associate a specific environment (i.e., the context) and a sound (i.e., the cue) with electric foot shocks. The fear memory is manifested by the mouse freezing when it is subsequently exposed to this specific context or cue without electric shocks. At two tested ages, *Stxbp1*^{tm1d/+} and *Stxbp1*^{tm1a/+} mice displayed a profound reduction in both context- and cue-induced freezing behaviors when tested 24 hours after the conditioning paradigm (**Figure 3B–E**). We also tested *Stxbp1*^{tm1d/+} mice 1 hour after the conditioning paradigm and observed similar deficits (**Figure 3-supplement 1E**). Since the acoustic startle response and nociception are intact in *Stxbp1* haploinsufficient mice (**Figure 2-supplement 2A,C**), these results indicate that *Stxbp1* haploinsufficiency impairs both hippocampus-dependent contextual and hippocampus-independent cued fear memories.

Finally, we used the Y maze spontaneous alternation test to examine working memory, but did not observe significant difference between *Stxbp1*^{tm1d/+} and WT mice (**Figure 3-supplement 1F**). Taken together, our results indicate that both long-term and short-term forms of recognition and associative memories are severely impaired in *Stxbp1* haploinsufficiency mice, but their working memory is intact.

***Stxbp1* haploinsufficient mice exhibit an increase in anxiety-like and repetitive behaviors**

A number of psychiatric phenotypes including hyperactivity, anxiety, stereotypies, aggression, and autistic features were reported in subsets of *STXBP1* encephalopathy patients. We used a battery of behavioral assays to characterize each of these features in *Stxbp1* haploinsufficiency mice. The open-field test indicates that *Stxbp1* haploinsufficiency mice are hyperactive and more anxious than WT mice (**Figure 2A–E**). To specifically assess anxiety-like behaviors, we tested *Stxbp1*^{tm1d/+} and *Stxbp1*^{tm1a/+} mice in the elevated plus maze and light-dark chamber tests where a mouse is allowed to explore the open or closed arms of the maze and the clear or black chamber of the box, respectively. *Stxbp1*^{tm1d/+} and *Stxbp1*^{tm1a/+} mice entered the open arms and clear chamber less frequently and traveled shorter distance in the open arms and clear chamber than WT mice (**Figure 4A–D; Figure 4-supplement 1A–D**). Hence, these results confirm the heightened anxiety in *Stxbp1* haploinsufficient mice and are consistent with the previous studies (Hager et al., 2014; Miyamoto et al., 2017; Kovačević et al., 2018).

To assess the stereotyped and repetitive behaviors, we used the hole-board test to measure the pattern of mouse exploratory nose poke (also called head dipping) behavior. As compared to WT mice, *Stxbp1* haploinsufficient mice explored similar numbers of holes (**Figure 4E**) and made

similar or larger numbers of nose pokes (**Figure 4F**). We analyzed the repetitive nose pokes (i.e., ≥ 2 consecutive pokes) into the same hole as a measure of repetitive behaviors. The mutant mice made more repetitive nose pokes than WT mice across many holes (**Figure 4G**), indicating that *Stxbp1* haploinsufficiency in mice causes abnormal stereotypy and repetitive behaviors, a psychiatric feature observed in about 20% of the *STXBP1* encephalopathy patients (Stamberger et al., 2016).

Social aggression of *Stxbp1* haploinsufficient mice are elevated

During daily mouse husbandry, we noticed incidences of fighting and injuries of WT and *Stxbp1* haploinsufficient mice in their home cages, but no injuries were observed when *Stxbp1* haploinsufficient mice were singly housed, suggesting that the injuries likely resulted from fighting instead of self-injury. To formally examine aggressive behaviors, we first performed the resident-intruder test, in which a male intruder mouse is introduced into the home cage of a male resident mouse, and the aggressive behaviors of the resident towards the intruder were scored. As compared to WT mice, male resident *Stxbp1*^{tm1d/+} and *Stxbp1*^{tm1a/+} mice were more likely to attack and spent more time attacking the intruders (**Figure 5A–C**). Another paradigm to assess aggression and social dominance is the tube test, in which two mice are released into the opposite ends of a tube, and the more dominant and aggressive mouse will win the competition by pushing its opponent out of the tube. When *Stxbp1*^{tm1d/+} and *Stxbp1*^{tm1a/+} mice were placed against their sex- and age-matched WT littermates, *Stxbp1* haploinsufficient mice won more competitions despite their smaller body sizes (**Figure 5D**). Thus, *Stxbp1* haploinsufficiency elevates innate aggression in mice.

To further evaluate social interaction, we performed the three-chamber test where a mouse is allowed to interact with an object or a sex- and age-matched partner mouse. Like WT mice, *Stxbp1*^{tm1d/+} and *Stxbp1*^{tm1a/+} mice preferred to interact with the partner mice rather than the objects (**Figure 5E**), indicating that *Stxbp1* haploinsufficiency does not compromise general sociability. Interestingly, the mutant mice in fact spent significantly more time than WT mice interacting with the partner mice ($P < 0.0001$ for *Stxbp1*^{tm1d/+} vs. WT and $P = 0.0015$ for *Stxbp1*^{tm1a/+} vs. WT), which might be due to the increased aggression of the mutant mice. Furthermore, we used the partition test to examine the preference for social novelty, in which a mouse is allowed to interact with a familiar or novel partner mouse. Both WT and *Stxbp1*^{tm1d/+} mice preferentially interacted more with the novel partner mice (**Figure 5-supplement 1A**). These results indicate that the general sociability and interest in social novelty are normal in *Stxbp1* haploinsufficient mice.

Reduced nest building and digging behaviors in *Stxbp1* haploinsufficient mice

To further assess the well-being and psychiatric phenotypes of *Stxbp1* haploinsufficient mice, we performed the Nestlet shredding test and marble burying test to examine two innate behaviors, nest building and digging, respectively. We provided a Nestlet (pressed cotton square) to each mouse in the home cage and scored the degree of shredding and nest quality after 24, 48, and 72 hours (**Figure 5F**). *Stxbp1*^{tm1d/+} and *Stxbp1*^{tm1a/+} mice consistently scored lower than WT mice at all time points (**Figure 5G**). In the marble burying test, the *Stxbp1*^{tm1d/+} and *Stxbp1*^{tm1a/+} mice buried fewer marbles than WT mice (**Figure 5H**). The interpretation of marble burying remains controversial, as it may measure anxiety, compulsive-like behavior, or simply digging behavior (Deacon, 2006; Thomas et al., 2009; Wolmarans et al., 2016). Since *Stxbp1* haploinsufficient

mice show elevated anxiety and repetitive behaviors, the reduced marble burying likely reflects an impairment of digging behavior, possibly due to the motor deficits. Likewise, the motor deficits may also contribute to the reduced nest building behavior.

Cortical hyperexcitability and epileptic seizures in *Stxbp1* haploinsufficient mice

Another core feature of *STXBP1* encephalopathy is epilepsy with a broad spectrum of seizure types, such as epileptic spasm, focal, tonic, clonic, myoclonic, and absence seizures (Stamberger et al., 2016; Suri et al., 2017). To investigate if *Stxbp1* haploinsufficient mice have abnormal cortical activity and epileptic seizures, we performed chronic video-electroencephalography (EEG) and electromyography (EMG) recordings in freely moving *Stxbp1*^{tm1d/+} mice and their sex- and age-matched WT littermates. We implanted three EEG electrodes in the frontal and somatosensory cortices and an EMG electrode in the neck muscles to record intracranial EEG and EMG, respectively, for at least 72 hours (**Figure 6A**). The phenotypes of each mouse are summarized in **Supplementary File 1**. *Stxbp1*^{tm1d/+} mice exhibited cortical hyperexcitability and several epileptiform activities. First, they had numerous spike-wave discharges (SWDs) that typically were 3–6 Hz and lasted 1–2 s (**Figure 6C,E,F**). These oscillations showed similar characteristics to those generalized spike-wave discharges observed in animal models of absence seizures (Maheshwari and Noebels, 2014; Depaulis and Charpier, 2018). A much smaller number of SWDs with similar characteristics were also observed in WT mice (**Figure 6B**), consistent with previous studies (Arain et al., 2012; Letts et al., 2014). On average, the frequency of SWD episodes in *Stxbp1*^{tm1d/+} mice was more than 40-fold higher than that in WT mice (**Figure 6E,F**). Importantly, SWDs frequently occurred in a cluster manner (i.e., ≥ 5 episodes with an inter-episode-interval of ≤ 60 s) in *Stxbp1*^{tm1d/+} mice, which never occurred in WT mice

(**Figure 6-supplement 1; Video 1**). Furthermore, 56 episodes of SWDs from 10 out of 13 *Stxbp1^{tm1d/+}* mice lasted more than 4 s, among which 54 episodes occurred during rapid eye movement (REM) sleep (**Figure 6D; Video 2**) and the other 2 episodes occurred when mice were awake. In contrast, only 1 out of 11 WT mice had 3 episodes of such long SWDs, all of which occurred when mice were awake (**Supplementary File 1**). In *Stxbp1^{tm1d/+}* mice, SWDs were most frequent during the night, but occurred throughout the day and night (**Figure 6F**), indicating a general cortical hyperexcitability and abnormal synchrony in *Stxbp1* haploinsufficient mice.

Second, *Stxbp1^{tm1d/+}* mice experienced frequent myoclonic seizures that manifested as sudden jumps or more subtle, involuntary muscle jerks associated with EEG discharges (**Figure 6G,H**). The large movement artifacts associated with the myoclonic jumps precluded proper interpretation of EEG signals, but this type of myoclonic seizures was observed in all 13 recorded *Stxbp1^{tm1d/+}* mice and the majority of episodes occurred during REM or non-rapid eye movement (NREM) sleep (**Figure 6I; Video 3**). There were 3 similar jumps in 2 out of 11 WT mice that were indistinguishable from those in *Stxbp1^{tm1d/+}* mice, but all of them occurred when mice were awake (**Figure 6I**). Moreover, the more subtle myoclonic jerks occurred frequently and often in clusters in *Stxbp1^{tm1d/+}* mice, whereas only isolated events were observed in WT mice at a much lower frequency (**Figure 6H,J; Video 4**). EEG and EMG recordings showed that the cortical EEG spikes associated with the myoclonic jerks occurred before or simultaneously with the neck muscle EMG discharges (**Figure 6H**), consistent with the cortical or subcortical origins of myoclonuses, respectively (Avanzini et al., 2016).

Normal cortical neuron densities in *Stxbp1* haploinsufficient mice

To identify cellular mechanisms that may underlie the cortical hyperexcitability and neurological deficits in *Stxbp1* haploinsufficient mice, we first examined the general cytoarchitecture and neuronal densities in the somatosensory cortex, as *Stxbp1* affects neuronal survival and migration (Verhage et al., 2000; Hamada et al., 2017). Immunostaining of a pan-neuronal marker NeuN revealed a grossly normal cytoarchitecture and cortical lamination in adult *Stxbp1*^{tm1d/+} mice (**Figure 7A,B**). The densities of cortical neurons and two major classes of inhibitory neurons, Pv and Sst interneurons, were similar between *Stxbp1*^{tm1d/+} and WT mice (**Figure 7B–D**). Thus, *Stxbp1* haploinsufficiency does not appear to affect cortical neuron survival and migration.

Stxbp1 haploinsufficiency reduces cortical inhibition in a synapse-specific manner

We next examined neuronal excitability and synaptic transmission in the somatosensory cortex. Whole-cell current clamp recordings of layer 2/3 pyramidal neurons in acute brain slices revealed only a small increase in the input resistances of *Stxbp1*^{tm1d/+} neurons as compared to WT neurons (**Figure 8-supplement 1**). Previous studies showed that synaptic transmission was reduced in the cultured hippocampal neurons from heterozygous *Stxbp1* knockout mice and human neurons derived from heterozygous *STXBP1* knockout embryonic stem cells (Toonen et al., 2006; Patzke et al., 2015; Orock et al., 2018). However, such a decrease in excitatory transmission onto excitatory neurons is probably inadequate to explain how *Stxbp1* haploinsufficiency *in vivo* leads to cortical hyperexcitability. Genetic deletion of one copy of *Stxbp1* from GABAergic neurons led to early lethality in a subset of mice, suggesting a crucial role of *Stxbp1* in GABAergic neurons ((Kovačević et al., 2018), but see (Miyamoto et al., 2017;

2019)). Thus, we focused on the inhibitory synaptic transmission originating from Pv and Sst interneurons. A Cre-dependent tdTomato reporter line, *Rosa26-CAG-LSL-tdTomato* (Madisen et al., 2010), and *Pv-ires-Cre* (Hippenmeyer et al., 2005) or *Sst-ires-Cre* (Taniguchi et al., 2011) were used to identify Pv or Sst interneurons, respectively. We used whole-cell current clamp to stimulate a single Pv or Sst interneuron in layer 2/3 with a brief train of action potentials and whole-cell voltage clamp to record the resulting unitary inhibitory postsynaptic currents (uIPSCs) in a nearby pyramidal neuron (**Figure 8A,E**). The connectivity rate of Pv interneurons to pyramidal neurons was unaltered in *Stxbp1^{tm1d/+};Rosa26^{tdTomato/+};Pv^{Cre/+}* mice (**Figure 8B**), but the unitary connection strength was reduced by 45% as compared to *Stxbp1^{+/+};Rosa26^{tdTomato/+};Pv^{Cre/+}* mice (**Figure 8C**). In contrast, *Stxbp1^{tm1d/+};Rosa26^{tdTomato/+};Sst^{Cre/+}* mice showed a 26% reduction in the connectivity rate of Sst interneurons to pyramidal neurons (**Figure 8F**), but the unitary connection strength was normal (**Figure 8G**). The short-term synaptic depression of both inhibitory connections during the train of stimulations was normal (**Figure 8D,H**). The inter-soma distances of interneurons and pyramidal neurons were similar between WT and mutant mice (Pv: WT $35.2 \pm 2.4 \mu\text{m}$, $n = 33$, mutant $33.2 \pm 2.5 \mu\text{m}$, $n = 31$, $P = 0.69$; Sst: WT $31.4 \pm 2.4 \mu\text{m}$, $n = 36$, mutant $32.0 \pm 2.1 \mu\text{m}$, $n = 36$, $P = 0.65$). Furthermore, we recorded the spontaneous excitatory postsynaptic currents (sEPSCs) in Pv and Sst interneurons and did not observe any significant changes of either amplitude or frequency in the mutant mice (**Figure 8-supplement 2**), suggesting that the excitatory drive onto interneurons is normal in *Stxbp1* haploinsufficient mice.

To determine the properties of quantal inhibitory transmission, we developed a new optogenetic method to isolate quantal IPSCs mediated by the GABA release specifically from Pv or Sst

interneurons. We expressed a blue light-gated cation channel, channelrhodopsin-2 (ChR2) (Nagel et al., 2003; Boyden et al., 2005; Li et al., 2005), in Pv interneurons by injecting a Cre recombinase-dependent adeno-associated virus (AAV) into the somatosensory cortices of *Stxbp1^{tm1d/+};Pv^{Cre/+}* and *Stxbp1^{+/+};Pv^{Cre/+}* mice (**Figure 9A**). We recorded miniature IPSCs (mIPSCs) from layer 2/3 pyramidal neurons in the presence of voltage-gated sodium channel blocker, tetrodotoxin (TTX), but without any voltage-gated potassium channel blockers. Under such conditions light activation of ChR2 did not evoke synchronous neurotransmitter release, but could enhance asynchronous exocytosis of synaptic vesicles from Pv interneurons, resulting in an increase in the frequency of mIPSCs (**Figure 9B**). We also replaced the extracellular Ca^{2+} with Sr^{2+} to further reduce the likelihood of synchronous release. Instead of using a constant light intensity, we gradually decreased the photostimulation strength to minimize the tonic currents (**Figure 9-supplement 1**). We mathematically subtracted the mIPSCs recorded during the baseline period (i.e., before blue light stimulation) from those recorded during blue light stimulation to obtain the average amplitude, charge, and decay time constant of Pv interneurons-mediated quantal IPSCs (**Figure 9B**), which were all similar between *Stxbp1^{tm1d/+};Pv^{Cre/+}* and *Stxbp1^{+/+};Pv^{Cre/+}* mice (**Figure 9E**). Using this optogenetic method, we also found that the average amplitude, charge, and decay time constant of quantal IPSCs mediated by Sst interneurons were normal in *Stxbp1^{tm1d/+};Sst^{Cre/+}* mice (**Figure 9C,D,F**). Thus, *Stxbp1* haploinsufficiency does not affect the postsynaptic properties of inhibitory transmission.

Altogether, our results indicate that the reduction in the strength of Pv interneuron synapses is most likely due to a decrease in the number of readily releasable vesicles or release probability because the quantal amplitude and connectivity are unaltered in *Stxbp1^{tm1d/+}* mice. Since Sst

interneuron density and overall neuron density are normal in *Stxbp1*^{tm1d/+} mice (**Figure 7**), a reduction in the connectivity rate of Sst interneurons to pyramidal neurons suggests a decrease in the number of inhibitory inputs onto pyramidal neurons. Thus, cortical inhibition mediated by both Pv and Sst interneurons is impaired in *Stxbp1* haploinsufficient mice, representing a likely cellular mechanism for the cortical hyperexcitability, seizures, and neurobehavioral deficits.

Discussion

Extensive biochemical and structural studies of Stxbp1/Munc18-1 have elucidated its crucial role in synaptic vesicle exocytosis (Rizo and Xu, 2015), but provided little insight into its functional role at the organism level. Hence, apart from being an essential gene, the significance of *STXBP1* dysfunction *in vivo* was not appreciated until its *de novo* heterozygous mutations were discovered first in epileptic encephalopathies (Saitsu et al., 2008) and later in other neurodevelopmental disorders (Hamdan et al., 2009; 2011; Rauch et al., 2012; Deciphering Developmental Disorders Study, 2015). In this study, we generated two new lines of *Stxbp1* haploinsufficient mice (*Stxbp1*^{tm1d/+} and *Stxbp1*^{tm1a/+}) and systematically characterized them in all of the neurologic and psychiatric domains affected by *STXBP1* encephalopathy. These mice exhibit reduced survival, hindlimb claspings, impaired motor coordination, learning and memory deficits, hyperactivity, increased anxiety-like and repetitive behaviors, aggression, and epileptic seizures. Sensory abnormality has not been documented in *STXBP1* encephalopathy patients (Stamberger et al., 2016) and we also did not observe any sensory dysfunctions in *Stxbp1* haploinsufficient mice. Thus, despite the large phenotypic spectrum of *STXBP1* encephalopathy in humans, our *Stxbp1* haploinsufficient mice recapitulate all key features of this neurodevelopmental disorder and are construct and face valid models of *STXBP1*

encephalopathy. Importantly, the identical phenotypes of *Stxbp1*^{tm1d/+} and *Stxbp1*^{tm1a/+} mice demonstrate the robustness and reproducibility of these preclinical models, providing a foundation to further study the disease pathogenesis and explore therapeutic strategies. About 17% of the *STXBP1* encephalopathy patients showed autistic traits (Stamberger et al., 2016), but we and others (Miyamoto et al., 2017; Kovačević et al., 2018) did not observe an impairment of social interaction in mutant mice using the three-chamber and partition tests. Perhaps the elevated aggression in *Stxbp1* haploinsufficient mice confounds these tests, or new mouse models that more precisely mimic the genetic alterations in the subset of *STXBP1* encephalopathy patients with autistic features are required to recapitulate this social behavioral phenotype.

Prior studies using the other three lines of *Stxbp1* heterozygous knockout mouse models reported only a subset of the neurologic and psychiatric deficits that we observed here (**Supplementary File 2**). For example, the reduced survival, hindlimb clasping, motor dysfunction, and increased repetitive behavior were not documented in the previous models. The previously reported cognitive phenotypes were much milder than what we observed. Both *Stxbp1*^{tm1d/+} and *Stxbp1*^{tm1a/+} mice showed severe impairments in the novel object recognition and fear conditioning tests. In contrast, another line of *Stxbp1* heterozygous knockout mice showed normal spatial learning in the Morris water maze and Barnes maze (a dry version of the spatial maze) in one study (Kovačević et al., 2018), but reduced spatial learning and memory in the radial arm water maze in another study (Orock et al., 2018). Different behavioral tests could have contributed to such differences among studies. However, a subtle but perhaps key difference is the *Stxbp1* protein levels in different lines of heterozygous mutant mice. *Stxbp1* is reduced by

40–50% in most brain regions of our *Stxbp1^{tm1d/+}* and *Stxbp1^{tm1a/+}* mice, but only by 25–50% in previous heterozygous knockout mice (Miyamoto et al., 2017; Orock et al., 2018), which may lead to fewer or less severe phenotypes. Furthermore, our study utilized much larger cohorts of mice for phenotypic characterization than previous studies, which allowed us to more comprehensively detect neurologic and psychiatric deficits in *Stxbp1^{tm1d/+}* and *Stxbp1^{tm1a/+}* mice.

Dysfunction of cortical GABAergic inhibition has been widely considered as a primary defect in animal models of autism spectrum disorder, schizophrenia, Down syndrome, and epilepsy among other neurological disorders (Ramamoorthi and Lin, 2011; Marín, 2012; Nelson and Valakh, 2015; Paz and Huguenard, 2015; Contestabile et al., 2017; Lee et al., 2017). In many cases, the origins of GABAergic dysfunction were either unidentified or attributed to Pv interneurons. Sst interneurons have only been directly implicated in a few disease models (Ito-Ishida et al., 2015; Rubinstein et al., 2015) despite their important physiological functions. Here we identified distinct deficits at Pv and Sst interneuron synapses in *Stxbp1* haploinsufficient mice, suggesting that *Stxbp1* may have diverse functions at distinct synapses. The reduction in the strength of Pv interneuron synapses is consistent with the previous results that basal synaptic transmission is reduced at the neuromuscular junctions of *Stxbp1* heterozygous null flies and mice (Wu et al., 1998; Toonen et al., 2006) and the glutamatergic synapses of human *STXBP1* heterozygous knockout neurons (Patzke et al., 2015). The reduced synaptic strength is likely due to a decrease in the number of readily releasable vesicles or release probability given the crucial role of *Stxbp1* in synaptic vesicle priming and fusion (Rizo and Xu, 2015) and the fact that the quantal amplitude and connectivity are normal in *Stxbp1^{tm1d/+}* mice. Although the short-term synaptic depression is unaltered in *Stxbp1^{tm1d/+}* mice, a change in release probability is still possible

because at the Pv interneuron synapses the short-term synaptic plasticity during a short train of action potentials is not sensitive to the release probability (Kraushaar and Jonas, 2000; Luthi et al., 2001). On the other hand, the reduction in the connectivity of Sst interneuron synapses is unexpected, as *Stxbp1* has not yet been implicated in the formation or maintenance of synapses. Complete loss of *Stxbp1* in mice does not appear to affect the initial formation of neural circuits, but causes cell-autonomous neurodegeneration and protein trafficking defects (Verhage et al., 2000; Heeroma et al., 2004; Law et al., 2016). Since *Munc13-1/2* double knockout mice also lack synaptic exocytosis, but do not show neurodegeneration (Varoqueaux et al., 2002), the degeneration phenotype in *Stxbp1* null mice is unlikely the result of total arrest of synaptic exocytosis. Thus, *Stxbp1* may regulate other intracellular processes in addition to presynaptic transmitter release, and we speculate that it may be involved in a protein trafficking process important for the formation or maintenance of Sst interneuron synapses. Future morphological and structural analyses of Sst interneuron synapses will be necessary to further confirm the involvement of *Stxbp1* in synapse formation or maintenance. Nevertheless, the impairment of Pv and Sst interneuron-mediated inhibition likely constitutes a key mechanism underlying the cortical hyperexcitability and neurobehavioral phenotypes of *Stxbp1* haploinsufficient mice. Future studies using cell-type specific *Stxbp1* haploinsufficient mouse models will help determine the role of specific GABAergic interneurons in the disease pathogenesis.

There are over one hundred developmental brain disorders that arise from mutations in postsynaptic proteins (Bayés et al., 2011; Deciphering Developmental Disorders Study, 2017), whereas few neurodevelopmental disorders have been diagnosed with mutations in presynaptic proteins until recently. In addition to *STXBPI*, pathogenic variants in genes encoding other key

components of the presynaptic neurotransmitter release machinery have been increasingly discovered in neurodevelopmental disorders. These include Ca^{2+} -sensor synaptotagmin 1 (*SYT1*), vesicle priming factor unc-13 homolog A (*UNC13A*), and all three components of the neuronal SNAREs, syntaxin 1B (*STX1B*), synaptosome associated protein 25 (*SNAP25*), and vesicle associated membrane protein 2 (*VAMP2*) (Rohena et al., 2013; Schubert et al., 2014; Shen et al., 2014; Baker et al., 2015; Engel et al., 2016; Hamdan et al., 2017; Lipstein et al., 2017; Baker et al., 2018; Fukuda et al., 2018; Salpietro et al., 2019; Wolking et al., 2019). Haploinsufficiency of these synaptic proteins is likely the leading disease mechanism because the majority of the cases were caused by heterozygous loss-of-function mutations. The clinical features of these disorders are diverse, but significantly overlap with those of *STXBP1* encephalopathy. The most common phenotypes are intellectual disability and epilepsy (or cortical hyperexcitability), which can be considered as the core features of these genetic synaptopathies. Thus, *Stxbp1* haploinsufficient mice are a valuable model to understand the cellular and circuit origins of these complex disorders and provide mechanistic insights into the growing list of neurodevelopmental disorders caused by synaptic dysfunction.

Materials and methods

Key resource table

Reagent type (species) or resource	Designation	Source or reference	Identifiers	Additional information

Cell line (<i>M. musculus</i>)	<i>Stxbp1</i> ^{tm1a} (EUCOMM)Hmgu embryonic stem cell clones (C57BL/6N strain)	European Conditional Mouse Mutagenesis Program (EUCOMM)	HEPD0510_5_A09, HEPD0510_5_B10	
Genetic reagent (<i>M. musculus</i>)	<i>Stxbp1</i> ^{tm1a} (C57BL/6J strain)	This paper		
Genetic reagent (<i>M. musculus</i>)	<i>Stxbp1</i> ^{tm1d} (C57BL/6J strain)	This paper		
Genetic reagent (<i>M. musculus</i>)	B6(Cg)- <i>Tyr</i> ^{c-2J} /J	The Jackson Laboratory	RRID:IMS R_JAX:000058	
Genetic reagent (<i>M. musculus</i>)	<i>Rosa26-Flpo</i> (C57BL/6J strain)	The Jackson Laboratory	RRID:IMS R_JAX:012930	
Genetic reagent (<i>M. musculus</i>)	<i>Sox2-Cre</i> (C57BL/6J strain)	The Jackson Laboratory	RRID:IMS R_JAX:008454	
Genetic reagent (<i>M. musculus</i>)	C57BL/6J	The Jackson Laboratory	RRID:IMS R_JAX:000664	
Genetic reagent (<i>M. musculus</i>)	<i>Pv-ires-Cre</i> (C57BL/6J strain)	The Jackson Laboratory	RRID:IMS R_JAX:017320	
Genetic reagent (<i>M. musculus</i>)	<i>Sst-ires-Cre</i> (C57BL/6;129S4 strain)	The Jackson Laboratory	RRID:IMS R_JAX:013044	
Genetic reagent (<i>M. musculus</i>)	<i>Rosa26-CAG-LSL-tdTomato</i> (C57BL/6J strain)	The Jackson Laboratory	RRID:IMS R_JAX:007914	
Antibody	Rabbit anti-Munc18-1, polyclonal	Abcam, catalog # ab3451	RRID:AB_303813	(1:2,000 or 1:5,000)
Antibody	Rabbit anti-Munc18-1, polyclonal	Synaptic Systems, catalog # 116002	RRID:AB_887736	(1:2,000 or 1:5,000)
Antibody	Rabbit anti-Gapdh, polyclonal	Santa Cruz Biotechnology, catalog #sc-25778	RRID:AB_10167668	(1:300 or 1:1,000)
Antibody	Goat anti-rabbit IgG conjugated with IRDye 680LT, polyclonal	LI-COR Biosciences, catalog # 925-68021	RRID:AB_2713919	(1:20,000)
Antibody	Rabbit anti-Somatostatin, polyclonal	Peninsula Laboratories International, catalog # T4103.0050	RRID:AB_518614	(1:3,000)

Antibody	Mouse anti-Parvalbumin, monoclonal	EMD Millipore, catalog # MAB1572	RRID:AB_2174013	(1:1,000)
Antibody	Guinea pig anti-NeuN, polyclonal	Sigma Millipore, catalog # ABN90	RRID:AB_11205592	(1:1,000)
Antibody	Goat anti-guinea pig IgG (H+L) conjugated with Alexa Flour 488, polyclonal	Invitrogen, catalog # A-11073	RRID:AB_2534117	(1:1,000)
Antibody	Goat anti-mouse IgG (H+L) conjugated with Alexa Flour 555, polyclonal	Invitrogen, catalog # A-21424	RRID:AB_141780	(1:1,000)
Antibody	Goat anti-rabbit IgG (H+L) conjugated with Alexa Flour 647, polyclonal	Invitrogen, catalog # A-21245	RRID:AB_141775	(1:1,000)
Recombinant DNA reagent	pAAV-EF1 α -DIO-hChR2(H134R)-P2A-EYFP	This paper	Addgene: 139283	This plasmid was used to produce the AAV vector used in Figure 9.
Transfected construct	AAV9-EF1 α -DIO-hChR2(H134R)-P2A-EYFP	This paper, Baylor College of Medicine Gene Vector Core	Addgene: 139283	This AAV vector was used in Figure 9.
Software, algorithm	Axograph X 1.5.4	AxoGraph	RRID:SCR_014284	https://axograph.com
Software, algorithm	pClamp 10.7	Molecular Devices	RRID:SCR_011323	https://www.moleculardevices.com
Software, algorithm	Image Studio Lite 5.0	LI-COR Biosciences	RRID:SCR_013715	https://www.licor.com
Software, algorithm	MATLAB R2015 to R2017	MathWorks	RRID:SCR_001622	https://www.mathworks.com
Software, algorithm	Prism 6.0, 7.0, and 8.0	GraphPad	RRID:SCR_002798	https://www.graphpad.com
Software, algorithm	Spyder 3.3.6 with Anaconda	Spyder	RRID:SCR_017585	https://www.spyder-ide.org
Software, algorithm	Siren timer 1.7.2 to 1.8.3	Pinnacle Technology	RRID:SCR_016183	https://www.pinnaclelet.com
Software, algorithm	Imaris 9.2	Oxford Instruments	RRID:SCR_007370	https://imaris.oxinst.com

Mice

Stxbp1^{tm1a(EUCOMM)Hmgu} embryonic stem (ES) cell clones (C57Bl/6N strain) were obtained from the European Conditional Mouse Mutagenesis Program (EUCOMM) and the targeting was

531 confirmed by Southern blots. Two ES cell clones (HEPD0510_5_A09 and HEPD0510_5_B10)
 532 were injected into blastocysts to generate chimeric mice. Germline transmission of clone
 533 HEPD0510_5_A09 was obtained by crossing chimeric mice to B6(Cg)-*Tyr^{c-2J}*/J mice (JAX
 534 #000058) to establish the KO-first (*tm1a*) line. Heterozygous KO-first mice were crossed to
 535 *Rosa26-Flpo* mice (Raymond and Soriano, 2007) to remove the trapping cassette in the germline.
 536 The resulting offspring were then crossed to *Sox2-Cre* mice (Hayashi et al., 2002) to delete exon
 537 7 in the germline to generate the KO (*tm1d*) line. Both *Rosa26-Flpo* and *Sox2-Cre* mice were
 538 obtained from the Jackson Laboratory (#012930 and 008454, respectively). *Stxbp1* mice were
 539 genotyped by PCR using primer sets 5'-TTCCACAGCCCTTTACAGAAAGG-3' and 5'-
 540 ATGTGTATGCCTGGACTCACAGGG-3' for WT allele, 5'-
 541 TTCCACAGCCCTTTACAGAAAGG-3' and 5'-CAACGGGTTCTTCTGTTAGTCC-3' for
 542 KO-first allele, and 5'-TTCCACAGCCCTTTACAGAAAGG-3' and 5'-
 543 TGAAGTATGGCGAGCTCAGACC-3' for KO allele.
 544
 545 Heterozygous *Stxbp1* KO-first and KO mice were crossed to wild type (WT) C57BL/6J mice
 546 (JAX #000664) for maintaining both lines on the C57BL/6J background and for generating
 547 experimental cohorts. Male BALB/cAnNTac mice were obtained from Taconic (#BALB-M). *Pv-*
 548 *ires-Cre* (Hippenmeyer et al., 2005), *Sst-ires-Cre* (Taniguchi et al., 2011), and *Rosa26-CAG-*
 549 *LSL-tdTomato* (Madisen et al., 2010) mice were obtained from the Jackson Laboratory (#017320,
 550 013044, and 007914, respectively). *Pv-ires-Cre* and *Rosa26-CAG-LSL-tdTomato* mice were
 551 maintained on the C57BL/6J background. *Sst-ires-Cre* mice were on a C57BL/6;129S4
 552 background. Heterozygous KO mice were crossed to *Rosa26-CAG-LSL-tdTomato* mice to
 553 generate *Stxbp1^{tm1d/+};Rosa26^{tdTomato/tdTomato}* mice. *Pv-ires-Cre* and *Sst-ires-Cre* mice were then

crossed to *Stxbp1*^{tm1d/+};*Rosa26*^{tdTomato/tdTomato} mice to generate
Stxbp1^{tm1d/+};*Rosa26*^{tdTomato/+};*Pv*^{Cre/+} or *Stxbp1*^{+/+};*Rosa26*^{tdTomato/+};*Pv*^{Cre/+} and
Stxbp1^{tm1d/+};*Rosa26*^{tdTomato/+};*Sst*^{Cre/+} or *Stxbp1*^{+/+};*Rosa26*^{tdTomato/+};*Sst*^{Cre/+} mice, respectively. *Pv-*
ires-Cre and *Sst-ires-Cre* mice were also crossed to *Stxbp1*^{tm1d/+} mice to generate
Stxbp1^{tm1d/+};*Pv*^{Cre/+} or *Stxbp1*^{+/+};*Pv*^{Cre/+} and *Stxbp1*^{tm1d/+};*Sst*^{Cre/+} or *Stxbp1*^{+/+};*Sst*^{Cre/+} mice,
respectively.

Mice were housed in an Association for Assessment and Accreditation of Laboratory Animal
Care International-certified animal facility on a 14-hour/10-hour light/dark cycle. All procedures
to maintain and use mice were approved by the Institutional Animal Care and Use Committee at
Baylor College of Medicine.

Southern and Western blots

Southern and Western blot analyses were performed according standard protocols. For Southern
blots, genomic DNA was extracted from ES cells and digested with BspHI for the 5' probe or
MfeI for the 3' probe (**Figure 1-supplement 1A**). ³²P-labeled probes were used to detect DNA
fragments. For Western blots, proteins were extracted from the brains at embryonic day 17.5 or 3
months of age using lysis buffer containing 50 mM Tris-HCl (pH 7.6), 150 mM NaCl, 1 mM
EDTA, 1% Triton X-100, 0.5% Na-deoxycholate, 0.1% SDS, and 1 tablet of cOmplete™, Mini,
EDTA-free Protease Inhibitor Cocktail (Roche) in 10 ml buffer. *Stxbp1* was detected by a rabbit
antibody against the N terminal residues 58–70 (Abcam, catalog # ab3451, lot # GR79394-18,
1:2,000 or 1:5,000 dilution) or a rabbit antibody against the C terminal residues 580–594
(Synaptic Systems, catalog # 116002, lot # 116002/15, 1:2,000 or 1:5,000 dilution). *Gapdh* was

detected by a rabbit antibody (Santa Cruz Biotechnology, catalog # sc-25778, lot # A0515, 1:300 or 1:1,000 dilution). Primary antibodies were detected by a goat anti-rabbit antibody conjugated with IRDye 680LT (LI-COR Biosciences, catalog # 925-68021, lot # C40917-01, 1:20,000 dilution). Proteins were visualized and quantified using an Odyssey CLx Imager and Image Studio Lite 5.0 (LI-COR Biosciences).

Immunohistochemistry and fluorescent microscopy

Mice were anesthetized by an intraperitoneal injection of a ketamine and xylazine mix (80 mg/kg and 16 mg/kg, respectively) and transcardially perfused with phosphate buffered saline (PBS, pH 7.4) followed by 4% paraformaldehyde in PBS (pH 7.4). Brains were then post-fixed for two hours in 4% paraformaldehyde at 4°C, cryoprotected with 30% sucrose, and sectioned into 50 µm coronal slices using a HM 450 Sliding Microtome (Thermo Scientific). Brain sections were stored in an ethylene glycol:glycerol:PBS solution (1:1:1.3) until use. Sections containing the somatosensory cortex were incubated in blocking solution (0.2% Triton X-100 in PBS with 10% normal goat serum) for 2 hours and then with primary antibodies for 48 hours at 4°C. Primary antibodies were diluted to the following concentrations in blocking solution: rabbit anti-Somatostatin (Peninsula Laboratories International, catalog # T4103.0050, lot # A17908, 1:3000), mouse anti-Parvalbumin (EMD Millipore, catalog # MAB1572, lot # 2982272, 1:1000), and guinea pig anti-NeuN (Sigma Millipore, catalog # ABN90, lot # 3253333, 1:1000). Sections were washed in 0.2% Triton X-100 in PBS and then incubated with the following secondary antibodies diluted 1:1000 in blocking solution for 24 hours at 4°C: goat anti-guinea pig IgG (H+L) conjugated with Alexa Flour 488 (Invitrogen, catalog # A-11073, lot # 1841755), goat anti-mouse IgG (H+L) conjugated with Alexa Flour 555 (Invitrogen, catalog # A-21424, lot #

1588453), goat anti-rabbit IgG (H+L) conjugated with Alexa Flour 647 (Invitrogen, catalog # A-21245, lot # 1623067). Sections were washed in 0.2% Triton X-100 in PBS and mounted in ProLong Diamond Antifade Mountant with DAPI (Invitrogen, catalog # P36962).

Low magnification images of brain sections were acquired on an Axio Zoom.V16 Fluorescence Stereo Zoom Microscope (Zeiss). High magnification, tile scanned z-stack images of the primary somatosensory cortex were acquired on an Sp8X Confocal Microscope (Leica) using a 20× oil objective. Three brain sections were imaged and quantified per mouse. Approximately 50 images were acquired per tile scan with a 5% overlap between images for tiling. The z-stack was centered in the middle of the brain section and 10 optical sections were taken at 0.39-μm step. For analysis, the 3 optical sections in the middle of the z-stack were processed using the “Sum Slices” function in ImageJ (National Institutes of Health) and then the images were cropped to a region of approximately 2 mm² spanning all cortical layers. Within this region, each Pv or Sst interneuron was confirmed to be co-labeled with DAPI and NeuN and counted manually. The numbers of NeuN positive cells were estimated using the Surfaces function in Imaris 9.2 (Oxford Instruments) with the following parameters: surface grain size = 0.568 μm, eliminating background of largest sphere = 9 μm diameter, threshold = 30, seed point diameter = 7 μm, seed point quality = 10, and number of voxels < 200. Accuracy of surface detection was verified by manually counting NeuN positive cells in images containing about 200 cells and the error rate was less than 10%.

DNA construct, AAV production, and injection

Plasmid pAAV-EF1 α -DIO-hChR2(H134R)-P2A-EYFP was generated by replacing the hChR2(C128A H134R) in pAAV-EF1 α -DIO-hChR2(C128A H134R)-P2A-EYFP (Prakash et al., 2012) with the hChR2(H134R) from pAAV-EF1 α -DIO-hChR2(H134R)-EYFP (Addgene #20298) and was deposited at Addgene (#139283). The recombinant AAV vectors were produced by the Gene Vector Core at Baylor College of Medicine. To express ChR2 in Pv or Sst interneurons, 200 nl of AAV9-EF1 α -DIO-hChR2(H134R)-P2A-EYFP vectors (3×10^{13} genome copies/ml) were injected into the somatosensory cortex of *Stxbp1*^{tm1d/+};Pv^{Cre/+} and *Stxbp1*^{+/+};Pv^{Cre/+} or *Stxbp1*^{tm1d/+};Sst^{Cre/+} and *Stxbp1*^{+/+};Sst^{Cre/+} mice, respectively, at postnatal day 1–5 as previously described (Xue et al., 2014; Messier et al., 2018) with an UltraMicroPump III and a Micro4 controller (World Precision Instruments).

Behavioral tests

All behavioral experiments except the tube test were performed and analyzed blind to the genotypes. The numbers of mice needed were estimated based on previous studies using similar behavioral tests. Approximately equal numbers of *Stxbp1* mutant mice and their sex- and age-matched WT littermates of both sexes were tested in parallel in each experiment except the resident-intruder test where only male mice were used. In each cage, two mutant and two WT mice were housed together. Before all behavioral tests, mice were habituated in the behavioral test facility for at least 30 minutes. The sexes and ages of the tested mice were indicated in the figures.

Open-field test: A mouse was placed in the center of a clear, open chamber (40 × 40 × 30 cm) and allowed to freely explore for 30 minutes in the presence of 700–750-lux illumination and 65-

dB background white noise. In each chamber, two layers of light beams (16 for each layer) in the horizontal X and Y directions capture the locomotor activity of the mouse. The horizontal plane was evenly divided into 256 squares (16×16), and the center zone is defined as the central 100 squares (10×10). The horizontal travel and vertical activity were quantified by either an Open Field Locomotor system or a VersaMax system (OmniTech).

Rotarod test: A mouse was placed on an accelerating rotarod apparatus (Ugo Basile). Each trial lasted for a maximum of 5 minutes, during which the rod accelerated linearly from 4 to 40 revolutions per minute (RPM) or 8 to 80 RPM. The time when the mouse walks on the rod and the latency for the mouse to fall from the rod were recorded for each trial. Mice were tested in 4 trials per day for 2 consecutive days or in 3 trials per day for 4 consecutive days. There was a 30–60-minute resting interval between trials.

Dowel test: A mouse was placed in the center of a horizontal dowel (6.5-mm or 9.5-mm diameter) and the latency to fall was measured with a maximal cutoff time of 120 seconds.

Inverted screen test: A mouse was placed onto a wire grid, and the grid was carefully picked up and shaken a couple of times to ensure that the mouse was holding on. The grid was then inverted such that the mouse was hanging upside down from the grid. The latency to fall was measured with a maximal cutoff time of 60 seconds.

Wire hang test: A mouse was suspended by its forepaws on a 1.5-mm wire and the latency to fall was recorded with a maximal cutoff time of 60 seconds.

668

669 Foot slip test: A mouse was placed onto an elevated 40 × 25 cm wire grid (1 × 1 cm spacing) and
670 allowed to freely move for 5 minutes. The number of foot slips was manually counted, and the
671 moving distance was measured through a video camera (ANY-maze, Stoelting). The number of
672 foot slips were normalized by the moving distance for each mouse.

673

674 Vertical pole test: A mouse was placed head-upward at the top of a vertical threaded metal pole
675 (1.3-cm diameter, 55-cm length). The amount of time for the mouse to turn around and descend
676 to the floor was measured with a maximal cutoff time of 120 seconds.

677

678 Grip strength: Forelimb grip strength was measured using a Grip Strength Meter (Columbus
679 Instruments). A mouse was held by the tail and allowed to grasp a trapeze bar with its forepaws.
680 Once the mouse grasped the bar with both paws, the mouse was pulled away from the bar until
681 the bar was released. The digital meter displayed the level of tension exerted on the bar in gram-
682 force (gf).

683

684 Acoustic startle response test: A mouse was placed in a well-ventilated, clear plastic cylinder and
685 acclimated to the 70-dB background white noise for 5 minutes. The mouse was then tested with
686 4 blocks. Each block consisted of 13 trials, during which each of 13 different levels of sound (70,
687 74, 78, 82, 86, 90, 94, 98, 102, 106, 110, 114, or 118 dB, 40 milliseconds, inter-trial interval of
688 15 seconds on average) was presented in a pseudorandom order. The startle response was
689 recorded for 40 milliseconds after the onset of the sound. The rapid force changes due to the
690 startles were measured by an accelerometer (SR-LAB, San Diego Instruments).

691

692 Pre-pulse inhibition test: A mouse was placed in a well-ventilated, clear plastic cylinder and
693 acclimated to the 70-dB background noise for 5 minutes. The mouse was then tested with 6
694 blocks. Each block consisted of 8 trials in a pseudorandom order: a "no stimulus" trial (40
695 milliseconds, only 70-dB background noise present), a test pulse trial (40 milliseconds, 120 dB),
696 3 different pre-pulse trials (20 milliseconds, 74, 78, or 82 dB), and 3 different pre-pulse
697 inhibition trials (a 20-millisecond, 74, 78, or 82 dB pre-pulse preceding a 40-millisecond, 120-
698 dB test pulse by 100 milliseconds). The startle response was recorded for 40 milliseconds after
699 the onset of the 120-dB test pulse. The inter-trial interval is 15 seconds on average. The rapid
700 force changes due to the startles were measured by an accelerometer (SR-LAB, San Diego
701 Instruments). Pre-pulse inhibition of the startle responses was calculated as "1 – (pre-pulse
702 inhibition trial/test pulse trial)".

703

704 Hot plate test: A mouse was placed on a hot plate (Columbus Instruments) with a constant
705 temperature of 55 °C. The latency for the mouse to first respond with either a hind paw lick,
706 hind paw flick, or jump was measured. If the mouse did not respond within 45 seconds, then the
707 test was terminated, and the latency was considered to be 45 seconds.

708

709 Novel object recognition test: A mouse was first habituated in an empty arena (24 × 45 × 20 cm)
710 for 5 minutes before every trial. The habituated mouse was then placed into the testing arena
711 with two identical objects for the first three trials. In the fourth trial, the mouse was exposed to
712 the familiar object that it interacted during the previous three trials and a novel object. In the fifth
713 trial, the mouse was presented with the two original, identical objects. Each trial lasted 5 minutes.

The inter-trial interval was 24 hours or 5 minutes. In the modified version, *Stxbp1^{tm1d/+}* and WT mice were exposed to the objects for 10 and 5 minutes during each trial, respectively. The movement of mice was recorded by a video camera placed above the test arena. The amount of time that the mouse interacted with the objects (*T*) was recorded using a wireless keyboard (ANY-maze, Stoelting). The preference index of interaction was calculated as $T_{\text{novel object}} / (T_{\text{familiar object}} + T_{\text{novel object}})$.

Fear conditioning test: Pavlovian fear conditioning was conducted in a chamber (30 × 25 × 29 cm) that has a grid floor for delivering electrical shocks (Coulbourn Instruments). A camera above the chamber was used to monitor the mouse. During the 5-minute training phase, a mouse was placed in the chamber for 2 minutes, and then a sound (85 dB, white noise) was turned on for 30 seconds immediately followed by a mild foot shock (2 sec, 0.72 mA). The same sound and foot shock were repeated one more time 2 minutes after the first foot shock. After the second foot shock, the mouse stayed in the training chamber for 18 seconds before returning to its home cage. After 1 or 24 hours, the mouse was tested for the contextual and cued fear memories. In the contextual fear test, the mouse was placed in the same training chamber and its freezing behavior was monitored for 5 minutes without the sound stimulus. The mouse was then returned to its home cage. One to two hours later, the mouse was transferred to the chamber after it has been altered using plexiglass inserts and a different odor to create a new context for the cued fear test. After 3 minutes in the chamber, the same sound cue that was used in the training phase was turned on for 3 minutes without foot shocks while the freezing behavior was monitored. The freezing behavior was scored using an automated video-based system (FreezeFrame, Actimetrics). The freezing time (%) during the first 2 minutes of the training phase (i.e., before

the first sound) was subtracted from the freezing time (%) during the contextual fear test. The freezing time (%) during the first 3 minutes of the cued fear test (i.e., without sound) was subtracted from the freezing time (%) during the last 3 minutes of the cued fear test (i.e., with sound).

Y maze spontaneous alternation test: A mouse was placed in the center of a Y-shaped maze consisting of three walled arms ($35 \times 5 \times 10$ cm) and allowed to freely explore the different arms for 10 minutes. The sequence of the arms that the mouse entered was recorded using a video camera (ANY-maze, Stoelting). The correct choice refers to when the mouse entered an alternate arm after it came out of one arm.

Elevated plus maze test: A mouse was placed in the center of an elevated maze consisting of two open arms (25×8 cm) and two closed arms with high black walls ($25 \times 8 \times 15$ cm) and allowed to freely explore for 10 minutes in the presence of 700–750-lux illumination and 65-dB background white noise. The mouse activity was recorded using a video camera (ANY-maze, Stoelting).

Light-dark chamber test: A mouse was placed in a rectangular light-dark chamber ($44 \times 21 \times 21$ cm) and allowed to freely explore for 10 minutes in the presence of 700–750 lux illumination and 65-dB background white noise. One third of the chamber is made of black plexiglass (dark) and two thirds is made of clear plexiglass (light) with a small opening between the two areas. The movement of the mouse was tracked by the Open Field Locomotor system (OmniTech).

760 Hole-board test: A mouse was placed at the center of a clear chamber ($40 \times 40 \times 30$ cm) that
761 contains a black floor with 16 evenly spaced holes (5/8-inch diameter) arranged in a 4×4 array.
762 The mouse was allowed to freely explore for 10 minutes. Its open-field activity above the
763 floorboard and nose pokes into the holes were detected by infrared beams above and below the
764 hole board, respectively, using the VersaMax system (OmniTech).

765

766 Resident-intruder test: Male test mice (resident mice) were individually caged for 2 weeks before
767 testing, and age-matched male white BALB/cAnNTac mice (Taconic) were group-housed to
768 serve as the intruders. During the test, an intruder was placed into the home cage of a test mouse
769 for 10 minutes, and their behaviors were video recorded. Videos were scored for the number and
770 duration of each attack by the resident mouse regardless the attack was initiated by either the
771 resident or intruder.

772

773 Tube test: A pair of a mutant mouse and an age- and sex-matched WT littermate that were
774 housed in different home cages were placed into the opposite ends of a clear acrylic, cylindrical
775 tube (3.5-cm diameter). The mouse that retreats backwards first was considered as the loser. The
776 winner was scored as 1 and the loser as 0. Each mutant mouse was tested against 3 different WT
777 littermates and the scores were averaged.

778

779 Three-chamber test: The apparatus ($60.8 \times 40.5 \times 23$ cm) consists of three chambers (left, center,
780 and right) of equal size with 10×5 cm openings between the chambers. WT C57BL/6J mice
781 were used as partner mice. A test mouse was placed in the apparatus with a mesh pencil cup in
782 each of the left and right chambers and allowed to freely explore for 10 minutes. A novel object

was then placed under one mesh pencil cup and an age- and sex-matched partner mouse under the other mesh pencil cup. The test mouse was allowed to freely explore for another 10 minutes. The position of the test mouse was tracked through a video camera (ANY-maze, Stoelting), and the approaches of the test mouse to the object or partner mouse were scored manually using a wireless keyboard. Partner mice were habituated to the mesh pencil cups in the apparatus for 1 hour per day for 2 days prior to testing. A partner mouse was used only in one test per day.

Partition test: The partitioned cage is a standard mouse cage ($28.5 \times 17.5 \times 12$ cm) divided in half with a clear perforated partition (a hole of 0.6-cm diameter). WT C57BL/6J mice were used as partner mice. A test mouse was housed in one side of the partitioned cage for overnight. In the afternoon before testing, an age- and sex-matched partner mouse was placed in the opposite half of the partitioned cage. On the next day, the time and number of approaches of the test mouse to the partition were scored using a handheld Psion event recorder (Observer, Noldus) in three 5-minute tests. The first test measured the approaches with the familiar overnight partner. The second measured the approaches with a novel partner mouse. The third test measured the approaches with the returned original partner mouse.

Nestlet shredding test: A mouse was individually housed in its home cage, and an autoclaved Nestlet was given to the mouse. The quality of the nest was assessed every 24 hours for 3 consecutive days.

Marble burying test: A clean standard housing cage was filled with approximately 8-cm deep bedding material. 20 marbles were arranged on top of the bedding in a 4×5 array. A mouse was

placed into this cage and remained undisturbed for 30 minutes before returning to its home cage. The number of buried marbles (i.e., at least 2/3 of the marble covered by the bedding) was recorded.

Video-EEG/EMG

Mice at 3–4 weeks of age were anesthetized with 2.5% isoflurane in oxygen, and the body temperature was maintained by a feedback based DC temperature control system at 37°C. The head was secured in a stereotaxic apparatus, and an incision was made along the midline to expose the skull. Craniotomies (approximate diameter of 0.25 mm) were performed with a round bur (0.25-mm diameter) and a high-speed rotary micromotor at coordinates (see below) that were normalized by the distance between Bregma and Lambda (DBL). Perfluoroalkoxy polymer (PFA)-coated silver wire electrodes (127- μ m bare diameter, 177.8- μ m coated diameter, A-M Systems) were used for grounding, referencing, and recording. A grounding electrode was placed on the right frontal cortex. An EEG reference electrode was placed on the cerebellum. Three EEG electrodes were placed on the left frontal cortex (anterior posterior (AP): 0.42 of DBL, medial lateral (ML): 0.356 of DBL, dorsal ventral (DV): -1.5 mm), left, and right somatosensory cortices (AP: -0.34 of DBL, ML: \pm 0.653 of DBL, DV: -1.5mm). An EMG recording and an EMG reference electrode were inserted into the neck muscles. All the electrodes were connected to an adapter that was secured on the skull by dental acrylic. The skin around the wound was sutured, and mice were returned to the home cage to recover for at least one week. Before recording, mice were individually habituated in the recording chambers (10-inch diameter of plexiglass cylinder with bedding and access to food and water) for 24 hours. EEG/EMG signals were sampled at 5000 Hz with a 0.5-Hz high-pass filter, and synchronous videos were recorded

829 at 30 frames per second from freely moving mice for continuous 72 hours using a 4-channel
 830 EEG/EMG tethered system (Pinnacle Technology).
 831
 832 To detect spike-wave discharges (SWDs), EEG signals of each channel were divided into 10-
 833 minute segments, and each segment was filtered by a third order Butterworth bandpass filter with
 834 0.5–400 Hz cutoffs. The filtered data was divided into 250-millisecond non-overlapping epochs.
 835 EEG signal changes that occurred in the time domain were captured by root mean square
 836 ($RMS = \sqrt{\sum_{i=1}^{i=n} s_i^2 / n}$; s , EEG signal; $n = 1250$), and spike density (number of spikes normalized
 837 to each epoch). EEG signal changes that occurred in the frequency domain were captured by
 838 frequency band ratio ($FBR = \sum_{n=f1}^{n=f2} ABS(FFT(n)) / \sum_{n=f3}^{n=f4} ABS(FFT(n))$; $f1 = 100$; $f2 = 300$;
 839 $f3 = 0.5$; $f4 = 80$) where the power of the upper band (100–300 Hz) was contrasted with that of
 840 the lower band (0.5–80 Hz). The above features were computed in MATLAB. An EEG segment
 841 that exceeded thresholds for all of the above features was identified as a SWD candidate. The
 842 candidates were further classified by a convolutional neural network in Spyder (Spyder) that was
 843 trained with manually labeled EEG segments. The first layer of the network contained 32 filters
 844 that returned their matches with 10-millisecond (kernel size) non-overlapping (stride) candidate
 845 segments across the three EEG channels. Successive convolutional layers were stacked
 846 sequentially. For every two consecutive convolutional layers, there was a pooling layer that
 847 down-sampled the outputs by a factor of 5 to reduce computation. The overall network consisted
 848 of two layers of 32 filters, one layer of pooling, two layers of 64 filters, one layer of pooling, two
 849 layers of 128 filters, and one layer of pooling. The network was trained through an iterative
 850 approach. In each training iteration, the optimizer (Adadelata) updated the weights of the filters,
 851 and the loss function (binary cross entropy) evaluated how well the network predicted SWDs.

This iteration process continued until the loss function was minimized. Methods implemented to reduce overfitting included dropout (i.e., 50% of the neurons were randomly dropped out from calculation for each iteration) and early stopping (i.e., training process was stopped when the loss function on validation set did not decrease for 3 iterations). The trained neural network removed 99% of the false-positive candidates and the remaining candidates were further confirmed by visual inspection. For each SWD, the duration (the time difference between the first and last peaks) and spike rate were quantified. The SWD cluster was defined as a cluster of 5 or more SWD episodes that occurred with inter-episode-interval of maximal 60 s.

To identify myoclonic seizures, the EEG/EMG traces and videos were visually inspected to identify sudden jumps and myoclonic jerks. When the mouse suddenly and quickly move the body in less than one second, if one or more limbs leave the cage floor, then this is classified as a sudden jump. If all limbs stay on the cage floor, then this is classified as a myoclonic jerk. The state of the mouse right before the myoclonic seizure was classified as REM sleep, NREM sleep, or awake based on the EEG/EMG.

Brain slice electrophysiology

Mice were anesthetized by an intraperitoneal injection of a ketamine and xylazine mix (80 mg/kg and 16 mg/kg, respectively) and transcardially perfused with cold (0–4°C) slice cutting solution containing 80 mM NaCl, 2.5 mM KCl, 1.3 mM NaH₂PO₄, 26 mM NaHCO₃, 4 mM MgCl₂, 0.5 mM CaCl₂, 20 mM D-glucose, 75 mM sucrose and 0.5 mM sodium ascorbate (315 mosmol, pH 7.4, saturated with 95% O₂/5% CO₂). Brains were removed and sectioned in the cutting solution with a VT1200S vibratome (Leica) to obtain 300-μm coronal slices. Slices containing primary

875 somatosensory cortex were collected and incubated in a custom-made interface holding chamber
876 saturated with 95% O₂/5% CO₂ at 34 °C for 30 min and then at room temperature for 20 minutes
877 to 8 hours until they were transferred to the recording chamber.
878
879 Recordings were performed on submerged slices in artificial cerebrospinal fluid (ACSF)
880 containing 119 mM NaCl, 2.5 mM KCl, 1.3 mM NaH₂PO₄, 26 mM NaHCO₃, 1.3 mM MgCl₂,
881 2.5 mM CaCl₂, 20 mM D-glucose and 0.5 mM sodium ascorbate (305 mosmol, pH 7.4, saturated
882 with 95% O₂/5% CO₂, perfused at 3 ml/min) at 30–32°C. For whole-cell recordings, we used a
883 K⁺-based pipette solution containing 142 mM K⁺-gluconate, 10 mM HEPES, 1 mM EGTA, 2.5
884 mM MgCl₂, 4 mM ATP-Mg, 0.3 mM GTP-Na, 10 mM Na₂-phosphocreatine (295 mosmol, pH
885 7.35) or a Cs⁺-based pipette solution containing 121 mM Cs⁺-methanesulfonate, 1.5 mM MgCl₂,
886 10 mM HEPES, 10 mM EGTA, 4 mM Mg-ATP, 0.3 mM Na-GTP, 10 mM Na₂-Phosphocreatine,
887 and 2 mM QX314-Cl (295 mosmol, pH 7.35). Membrane potentials were not corrected for liquid
888 junction potential (experimentally measured as 12.5 mV for the K⁺-based pipette solution and
889 9.5 mV for the Cs⁺-based pipette solution).
890
891 Neurons were visualized with video-assisted infrared differential interference contrast imaging
892 and fluorescent neurons were identified by epifluorescence imaging under a water immersion
893 objective (40×, 0.8 numerical aperture) on an upright SliceScope Pro 1000 microscope
894 (Scientifica) with an infrared IR-1000 CCD camera (DAGE-MTI). Data were acquired at 10 kHz
895 and low-pass filtered at 4 kHz with an Axon Multiclamp 700B amplifier and an Axon Digidata
896 1550 or 1440 Data Acquisition System under the control of Clampex 10.7 (Molecular Devices).
897 For the photostimulation of ChR2-expressing neurons, blue light was emitted from a collimated

898 light-emitting diode (LED) of 455 nm. The LEDs were driven by a LED driver (Mightex) under
899 the control of an Axon Digidata 1550 Data Acquisition System and Clampex 10.7. Light was
900 delivered through the reflected light fluorescence illuminator port and the 40× objective.
901 Data were analyzed offline using Clampfit 10.7 (Molecular Devices) or AxoGraph X (AxoGraph
902 Scientific).
903
904 Neuronal intrinsic excitability was examined with the K^+ -based pipette solution. The resting
905 membrane potential was recorded in the whole-cell current clamp mode within the first minute
906 after break-in. After balancing the bridge, the input resistance was measured by injecting a 500-
907 ms hyperpolarizing current pulse (10–100 pA) to generate a small membrane potential
908 hyperpolarization (2–10 mV) from the resting membrane potential. Depolarizing currents were
909 increased in 5- or 10-pA steps to identify rheobase currents.
910
911 To record unitary connections between inhibitory interneurons and pyramidal neurons, Pv and
912 Sst interneurons were identified by the Cre-dependent expression of tdTomato. Pyramidal
913 neurons were first recorded in whole-cell voltage clamp mode at the reversal potential for
914 excitation (+10 mV) with the Cs^+ -based patch pipette solution. A nearby Pv or Sst interneuron
915 was subsequently recorded in the whole-cell current clamp mode with the K^+ -based patch pipette
916 solution. Action potentials were elicited in Pv or Sst interneurons by a train of 6 depolarizing
917 current steps (2 ms, 1–2 nA) at 10 Hz with 15-s intervals between sweeps. Unitary IPSC (uIPSC)
918 amplitudes were measured from the average of 30–50 sweeps. We considered a Pv or Sst
919 interneuron to be connected with a pyramidal neuron when the average uIPSC amplitude was at
920 least three times the baseline standard deviation. Spontaneous EPSCs (sEPSCs) in Pv and Sst

interneurons were recorded in whole-cell voltage clamp mode at the reversal potential for inhibition (-70 mV) with the K^+ -based patch pipette solution. To detect sEPSCs, data were digitally low-pass filtered at 2 kHz offline and events were detected by a scaled-template algorithm (AxoGraph X). The parameters of the template are: length, 5 ms; baseline, 1.5 ms; amplitude, -2 pA; rise time, 0.3 ms; and decay time, 0.7 ms. For voltage clamp experiments, only recordings with series resistance below 20 M Ω were included.

To isolate Pv or Sst interneurons-mediated quantal IPSCs, pyramidal neurons were recorded in whole-cell voltage clamp mode at the reversal potential for excitation ($+10$ mV) with the Cs^+ -based patch pipette solution in a modified ACSF containing 4 mM $MgCl_2$ and 0.5 mM $SrCl_2$ without $CaCl_2$. TTX (1 μ M), NBQX (10 μ M), and CPP (10 μ M) were also included in the modified ACSF to block synaptic excitation and reduce overall activity in the slices. Typically, 10–30 sweeps were recorded for each neuron with 40-s intervals between sweeps. During each sweep, mIPSCs were recorded during the 10-s baseline period and the 10-s blue light stimulation period. The light intensity (0.15–7.43 mW/mm²) was ramped down to reduce the tonic currents (**Figure 9-supplement 1**). To detect mIPSCs, data were digitally low-pass filtered at 2 kHz offline and events were detected by a scaled-template algorithm (AxoGraph X). The parameters of the template are: length, 20 ms; baseline, 3 ms; amplitude, 2 pA; rise time, 0.6 ms; and decay time, 10 ms. The average amplitude, charge, and decay time constant of quantal IPSCs from ChR2-expressing interneurons were computed as $A_{quantal} = (A_{light}f_{light} - A_{baseline}f_{baseline}) / (f_{light} - f_{baseline})$, where $A_{quantal}$, A_{light} , and $A_{baseline}$ are the amplitude, charge, or decay time constant of quantal IPSCs, mIPSCs during light stimulation period, and mIPSCs during baseline period, respectively; f_{light} and $f_{baseline}$ are the frequency of mIPSCs during light stimulation period

and that of mIPSCs during baseline period, respectively. The average traces of quantal IPSCs were computed similarly using the average traces of mIPSCs from the light stimulation period and baseline period. Only recordings with series resistance below 20 M Ω were included. Data were also excluded if blue light did not significantly evoke more mIPSCs than the baseline period (i.e., $P > 0.05$) or totally less than 150 evoked mIPSCs (i.e., the number of mIPSCs during the blue light stimulation period minus the number of mIPSCs during the baseline period) were obtained. The criterion of 150 evoked mIPSCs was chosen because the likelihood to accurately estimate the parameters (i.e., less than 10% error) from 150 events is higher than 95%.

Statistics

All reported sample numbers (n) represent independent biological replicates that are the numbers of tested mice or recorded neurons. Statistical analyses were performed with Prism 6, 7, or 8 (GraphPad Software). D'Agostino-Pearson, Shapiro-Wilk, and Kolmogorov-Smirnov tests were used to determine if data were normally distributed. If all data within one experiment passed all three normality tests, then the statistical test that assumes a Gaussian distribution was used. Otherwise, the statistical test that assumes a non-Gaussian distribution was used. All statistical tests were two-tailed with an alpha of 0.05. Gender effect was inspected by two-way or three-way ANOVA. The details of all statistical tests, numbers of replicates, and P values were reported in *Supplementary File 3*.

Acknowledgments

This article is dedicated to the memory of Caroline DeLuca, who inspired this project. We thank Gabriele Schuster for ES cell work and blastocyst injection, Corinne Spencer and James Frost for

suggestions and discussions, and Shuyun Deng and Kazuhiro Oka at the Baylor College of Medicine Gene Vector Core for recombinant AAV vector production. This work was supported in part by Citizens United for Research in Epilepsy (CURE Epilepsy Award to M.X.), the National Institutes of Health (R01NS100893 and R01MH117089 to M.X., F30MH118804 to C.M.L.), American Epilepsy Society (Postdoctoral Research Fellowship to W.C.), the Eunice Kennedy Shriver National Institute of Child Health and Human Development (U54HD083092 to Baylor College of Medicine Intellectual and Developmental Disabilities Research Center, Neurobehavioral Core), and the *In Vivo* Neurophysiology Core of Jan and Dan Duncan Neurological Research Institute. C.M.L. and J.E.M. are part of the Baylor College of Medicine Medical Scientist Training Program and McNair MD/PhD Student Scholars supported by the McNair Medical Institute at the Robert and Janice McNair Foundation. H.Y.Z. is a Howard Hughes Medical Institute investigator. M.X. is a Caroline DeLuca Scholar.

Legends

Figure 1. *Stxbp1* haploinsufficient mice exhibit reduced *Stxbp1* levels, survival, and body weights and develop hindlimb clasping.

(A) Genomic structures of *Stxbp1* WT, *tmla* (KO-first), and *tmld* (KO) alleles. In the *tmla* allele, the STOP including the *En2SA-lacZ-pA* trapping cassette (see **Figure 1-supplement 1A**) truncates the *Stxbp1* mRNA after exon 6. In the *tmld* allele, exon 7 is deleted, resulting in a premature stop codon in exon 8. E, exon; *FRT*, Flp recombination site; *loxP*, Cre recombination site. (B) Representative Western blots of proteins from different brain regions of 3-month-old WT, *Stxbp1^{tmld/+}*, and *Stxbp1^{tmla/+}* mice. Gapdh, a housekeeping protein as loading control. The brain regions are labeled by the same abbreviations as in (C). (C) Summary data of normalized *Stxbp1* expression levels from different brain regions. *Stxbp1* levels were first normalized by the Gapdh levels and then by the average *Stxbp1* levels of all WT mice from the same blot. Each filled (male) or open (female) circle represents one mouse. (D) *Stxbp1^{tmld/+}* and *Stxbp1^{tmla/+}* male mice were crossed with WT female mice. Pie charts show the observed genotypes of the offspring at weaning (i.e., around the age of 3 weeks). *Stxbp1^{tmld/+}* and *Stxbp1^{tmla/+}* mice were significantly less than Mendelian expectations. (E) *Stxbp1^{tmld/+}* and *Stxbp1^{tmla/+}* mice were smaller and showed hindlimb clasping (arrows). (F) Body weights as a function of age. M, male; F, female. (G) The fraction of mice with hindlimb clasping as a function of age. Bar graphs are mean \pm s.e.m. **, $P < 0.01$; ***, $P < 0.001$; ****, $P < 0.0001$.

Figure 1-supplement 1. Generation of two new *Stxbp1* null alleles.

(A) The *Stxbp1* WT genomic region was targeted by a multipurpose cassette that contains an *Engrailed 2* splice acceptor site (*En2SA*), an encephalomyocarditis virus internal ribosomal entry

site (*IRES*), *lacZ*, SV40 polyadenylation element (pA), and floxed exon 7, resulting in the KO-first allele (*tmla*). The restriction enzymes and probes used in the Southern blots are indicated in the diagrams. The KO-first allele was converted to the KO allele (*tmld*) by crossing *Stxbp1*^{*tmla/+*} mice with *Rosa26-Flpo* and *Sox2-Cre* mice sequentially. **(B)** Representative Western blots of *Stxbp1* and *Gapdh* proteins extracted from the brains at embryonic day 17.5. *Stxbp1* was detected by an antibody recognizing the C terminus (left two blots) or the N terminus (right two blots). The genotypes are indicated above the samples. Note that *Stxbp1* was reduced in heterozygous mutants and absent in homozygous mutants. **(C)** Summary data of normalized *Stxbp1* expression levels. *Stxbp1* levels were first normalized by the *Gapdh* levels and then by the average *Stxbp1* levels of all WT mice from the same blot. The data obtained by both *Stxbp1* antibodies are combined. Each triangle represents one mouse. Bar graphs are mean \pm s.e.m. **, $P < 0.01$; ***, $P < 0.001$; ****, $P < 0.0001$.

Figure 1-supplement 2. Reduced survival of *Stxbp1* haploinsufficient mice.

(A) *Stxbp1*^{*tmld/+*} and *Stxbp1*^{*tmla/+*} male mice were crossed with WT female mice. The observed genotypes of the offspring at weaning (i.e., around the age of 3 weeks) are shown in the pie charts. The male and female *Stxbp1*^{*tmld/+*} and *Stxbp1*^{*tmla/+*} mice were significantly less than Mendelian expectations. Note that the genotypes of some female mice were not determined and therefore, they were not included in this analysis. **(B)** Survival curves of a subset of *Stxbp1*^{*tmld/+*}, *Stxbp1*^{*tmla/+*}, and WT mice that were monitored for 80 weeks. The numbers of observed mice are indicated in the figures. n.s., $P > 0.05$; *, $P < 0.05$; **, $P < 0.01$; ****, $P < 0.0001$.

Figure 2. Motor dysfunctions of *Stxbp1* haploinsufficient mice.

(A) Representative tracking plots of the mouse positions in the open-field test. Note that *Stxbp1^{tm1d/+}* and *Stxbp1^{tm1a/+}* mice traveled less in the center (dashed box) than WT mice. (B–E) Summary data showing hyperactivity and anxiety-like behaviors of *Stxbp1^{tm1d/+}* and *Stxbp1^{tm1a/+}* mice in the open-field test. *Stxbp1^{tm1d/+}* and *Stxbp1^{tm1a/+}* mice showed an increase in the total moving distance (B) and speed (C), and a decrease in the ratio of center moving distances over total moving distance (D) and vertical activity (E). (F–H) *Stxbp1^{tm1d/+}* and *Stxbp1^{tm1a/+}* mice had weaker forelimb grip strength (F), made more foot slips per travel distance on a wire grid (G), and took more time to get down from a vertical pole (H). The numbers and ages of tested mice are indicated in the figures. Each filled (male) or open (female) circle represents one mouse. Bar graphs are mean \pm s.e.m. *, $P < 0.05$; **, $P < 0.01$; ***, $P < 0.001$; ****, $P < 0.0001$.

Figure 2-supplement 1. Normal performance of *Stxbp1^{tm1d/+}* mice in rotarod, dowel, inverted screen, and wire hang tests.

(A) In the 2-day rotarod test, 6–7-week old *Stxbp1^{tm1d/+}* mice performed better than WT mice, as they were able to walk (left panel) and stay (right panel) on the rotating rod for longer time, probably due to their lower body weights or hyperactivity. (B,C) Similar to (A), but for the ages of 26–27 weeks (B) and 61–69 weeks (C). *Stxbp1^{tm1d/+}* mice performed similar to WT mice. (D) In the 4-day rotarod test, *Stxbp1^{tm1d/+}* mice performed similar to WT mice at the age of 10–11 weeks. (E,F) *Stxbp1^{tm1d/+}* mice could stay on the dowel (6.5- or 9.5-mm diameter) for similar amount of time as WT mice. (G,H) *Stxbp1^{tm1d/+}* mice could hang on the screen (G) or wire (H) for similar amount of time as WT mice. The numbers and ages of tested mice are indicated in the figures. Each filled (male) or open (female) circle represents one mouse. Bar graphs are mean \pm s.e.m. n.s., $P > 0.05$; *, $P < 0.05$; **, $P < 0.01$.

Figure 2-supplement 2. *Stxbp1* haploinsufficient mice have normal sensory functions.

(A) *Stxbp1*^{tm1d/+} and *Stxbp1*^{tm1a/+} mice showed similar acoustic startle responses as WT mice at different sound levels. (B) In the pre-pulse inhibition test, when a weak sound (74, 78, or 82 dB) preceded a loud sound (120 dB), *Stxbp1*^{tm1d/+} and *Stxbp1*^{tm1a/+} mice showed a similar reduction in the startle responses to the loud sound as WT mice. (C) In the hot plate test, *Stxbp1*^{tm1d/+} and *Stxbp1*^{tm1a/+} mice showed similar latencies in response to the high temperature as WT mice. The numbers and ages of tested mice are indicated in the figures. Each filled (male) or open (female) circle represents one mouse. Bar graphs are mean \pm s.e.m. n.s., $P > 0.05$.

Figure 3. Impaired cognition of *Stxbp1* haploinsufficient mice.

(A) In the novel object recognition test with 24-hour testing intervals, the ability of a mouse to recognize the novel object was assessed by the preference index, which is the ratio between the time that the mouse interacts with the novel object and the total time that the mouse interacts with the familiar and novel objects. In contrast to WT mice, *Stxbp1*^{tm1d/+} and *Stxbp1*^{tm1a/+} mice did not show a preference for the novel object on day 4 when they were presented with the familiar and novel objects. (B–E) In the fear conditioning test, *Stxbp1*^{tm1d/+} and *Stxbp1*^{tm1a/+} mice at two different ages showed a reduction in both context-induced (B,D) and cue-induced (C,E) freezing behaviors 24 hours after training. The numbers and ages of tested mice are indicated in the figures. Each filled (male) or open (female) circle represents one mouse. Bar graphs are mean \pm s.e.m. ***, $P < 0.001$; ****, $P < 0.0001$.

Figure 3-supplement 1. *Stxbp1* haploinsufficient mice show an impairment in object

recognition and fear memory, but not working memory.

(A) In the novel object recognition test with 5-minute testing intervals, *Stxbp1*^{tm1d/+} mice did not show a preference for the novel object on trial 4 when they were presented with the familiar and novel objects. (B) In the novel object recognition test with 24-hour testing intervals (same as Figure 3A), *Stxbp1*^{tm1d/+} mice spent less time interacting with the familiar and novel objects. (C,D) In the modified novel object recognition test with 24-hour testing intervals, *Stxbp1*^{tm1d/+} mice spent similar amount of time interacting with the familiar and novel objects as WT mice (C), but they still failed to show a preference for the novel object on day 4 (D). (E) *Stxbp1*^{tm1d/+} mice showed a reduction in both contextual (left panel) and cued (right panel) fear memories 1 hour after training. (F) In the Y maze spontaneous alternation test that evaluates working memory, *Stxbp1*^{tm1d/+} mice made similar numbers of choices (left panel) and alternations (right panel) as WT mice. The numbers and ages of tested mice are indicated in the figures. Each filled (male) or open (female) circle represents one mouse. Bar graphs are mean \pm s.e.m. n.s., $P > 0.05$; *, $P < 0.05$; **, $P < 0.01$; ***, $P < 0.001$; ****, $P < 0.0001$.

Figure 4. *Stxbp1* haploinsufficient mice show increased anxiety-like and repetitive behaviors.

(A,B) In the elevated plus maze test, *Stxbp1*^{tm1d/+} and *Stxbp1*^{tm1a/+} mice entered the open arms less frequently (A) and traveled shorter distance in the open arms (B). (C,D) In the light-dark chamber test, *Stxbp1*^{tm1d/+} and *Stxbp1*^{tm1a/+} mice made less transitions between the light and dark chambers (C) and traveled shorter distance in the light chamber (D). (E–G) In the hole-board test, *Stxbp1*^{tm1d/+} and *Stxbp1*^{tm1a/+} mice poked similar numbers of holes as WT mice (E) and made similar or more total nose pokes (F). They made more repetitive nose pokes (i.e., ≥ 2 consecutive

pokes) than WT mice across different holes (G). The numbers and ages of tested mice are indicated in the figures. Each filled (male) or open (female) circle represents one mouse. Bar graphs are mean \pm s.e.m. n.s., $P > 0.05$; *, $P < 0.05$; **, $P < 0.01$; ***, $P < 0.001$.

Figure 4-supplement 1. The movements of *Stxbp1* haploinsufficient mice in elevated plus maze and light-dark chamber tests.

(A,B) In the elevated plus maze test, the total travel distances (A) and travel distances in the closed arms (B) of *Stxbp1*^{tm1d/+} and *Stxbp1*^{tm1a/+} mice were similar or slightly longer than those of WT mice. (C,D) In the light-dark chamber test, the total travel distances of *Stxbp1*^{tm1d/+} mice were reduced (C) due to the reduction of their travel distances in the light chamber and normal travel distances in the dark chamber (D). The total travel distances of *Stxbp1*^{tm1a/+} mice were normal (C) and their travel distances in the dark chamber was slightly increased as compared to WT mice (D). The numbers and ages of tested mice are indicated in the figures. Each filled (male) or open (female) circle represents one mouse. Bar graphs are mean \pm s.e.m. n.s., $P > 0.05$; *, $P < 0.05$; **, $P < 0.01$.

Figure 5. *Stxbp1* haploinsufficient mice show increased aggressive behaviors and reduced nest building and digging behaviors.

(A–C) In the resident-intruder test, male *Stxbp1*^{tm1d/+} and *Stxbp1*^{tm1a/+} mice showed a reduction in the latency to attack the male intruder mice (A). The total duration (B) and number (C) of their attacks were increased as compared to WT mice. (D) In the tube test, *Stxbp1*^{tm1d/+} and *Stxbp1*^{tm1a/+} mice won more competitions against their WT littermates. (E) In the three-chamber test, *Stxbp1*^{tm1d/+} and *Stxbp1*^{tm1a/+} mice showed a preference in interacting with the partner mouse

over the object. (F,G) *Stxbp1*^{tm1d/+} and *Stxbp1*^{tm1a/+} mice built poor quality nests. The quality of the nests was scored according to the criteria in (F) for 3 consecutive days (G). (H) *Stxbp1*^{tm1d/+} and *Stxbp1*^{tm1a/+} mice buried fewer marbles than WT mice. The numbers and ages of tested mice are indicated in the figures. Each filled (male) or open (female) circle represents one mouse. Bar graphs are mean \pm s.e.m. *, $P < 0.05$; **, $P < 0.01$; ***, $P < 0.001$; ****, $P < 0.0001$.

Figure 5-supplement 1. *Stxbp1* haploinsufficient mice show normal social interactions.

(A) In the partition test, *Stxbp1*^{tm1d/+} and WT mice showed a similar preference for the novel partner mouse over the familiar partner mouse. The numbers and ages of tested mice are indicated in the figures. Each filled (male) or open (female) circle represents one mouse. Bar graphs are mean \pm s.e.m. n.s., $P > 0.05$; **, $P < 0.01$; ***, $P < 0.001$; ****, $P < 0.0001$.

Figure 6. *Stxbp1*^{tm1d/+} mice exhibit cortical hyperexcitability and epileptic seizures.

(A–D) Representative EEG traces of the left frontal cortex (L-FC), left somatosensory cortex (L-SC), and right somatosensory cortex (R-SC), and EMG traces of the neck muscle from WT (A,B) and *Stxbp1*^{tm1d/+} mice (C,D). Spike-wave discharges (SWDs, indicated by the blue arrows) occurred frequently and often in a cluster manner in *Stxbp1*^{tm1d/+} mice (see **Video 1**). The grey line-highlighted SWDs from WT and *Stxbp1*^{tm1d/+} mice were expanded to show the details of the oscillations (B,C). A long SWD (i.e., > 4 s) during REM sleep from a *Stxbp1*^{tm1d/+} mouse is shown in (D) (see **Video 2**). (E) Summary data showing the overall SWD frequency (left panel), duration (middle panel), and average spike rate (right panel). (F) The numbers of SWDs per hour in WT (left Y axis) and *Stxbp1*^{tm1d/+} (right Y axis) mice are plotted as a function of time of day and averaged over 3 days. (G) Video frames showing a myoclonic jump from a *Stxbp1*^{tm1d/+}

1145 mouse (see **Video 3**). The mouse was in REM sleep before the jump. **(H)** Representative EEG
1146 and EMG traces showing myoclonic jerks (indicated by the blue arrows) from a *Stxbp1^{tm1d/+}*
1147 mouse (see **Video S4**). Two episodes of myoclonic jerks highlighted by the grey lines were
1148 expanded to show that the EEG discharges occurred prior to (the first episode) or simultaneously
1149 with (the second episode) the EMG discharges. **(I,J)** Summary data showing the frequencies of
1150 two types of myoclonic seizures in different behavioral states. The numbers and ages of recorded
1151 mice are indicated in the figures. Each filled (male) or open (female) circle represents one mouse.
1152 Bar graphs are mean \pm s.e.m. n.s., $P > 0.05$; **, $P < 0.01$; ***, $P < 0.001$; ****, $P < 0.0001$.

1153

1154 **Figure 6-supplement 1. The clustering of SWDs in *Stxbp1^{tm1d/+}* mice does not result from a**
1155 **random distribution of frequent SWD episodes.**

1156 **(A–C)** In *Stxbp1^{tm1d/+}* mice, many SWDs occurred in a cluster manner. A SWD cluster is defined
1157 as 5 or more episodes of SWDs that occur with an inter-episode-interval of 60 s or less. For each
1158 *Stxbp1^{tm1d/+}* mouse, simulations were performed to determine if the clustering of SWD episodes
1159 was simply due to the overall high frequencies of episodes. The recorded episodes of SWDs
1160 from a *Stxbp1^{tm1d/+}* mouse were randomly distributed in the same period of time for 10^6 times.
1161 The number of SWD clusters was determined from each simulated distribution, and the results of
1162 the 10^6 simulations are shown as the probability distribution of the number of SWD clusters for
1163 each mouse. The vertical lines with the same color as the probability distribution curves
1164 represent the numbers of the recorded SWD clusters in each mouse. The numbers of simulated
1165 SWD clusters are all smaller than that of recorded SWD clusters for each *Stxbp1^{tm1d/+}* mouse (P
1166 $< 10^{-6}$), demonstrating that a random distribution of the same number of SWD episodes does not
1167 result in the same clustering of SWDs in *Stxbp1^{tm1d/+}* mice.

Figure 7. Cortical neuron densities are unaltered in *Stxbp1*^{tm1d/+} mice.

(A) Representative fluorescent images of coronal sections stained by antibodies against NeuN (blue), Pv (green), and Sst (magenta). Note the similar cytoarchitecture between WT (upper panel) and *Stxbp1*^{tm1d/+} (lower panel) mice. (B) Representative fluorescent images of the somatosensory cortices within the boxed regions in (A) for WT (upper panels) and *Stxbp1*^{tm1d/+} (lower panels) mice. (C) Summary data showing similar densities of neurons (i.e., NeuN positive cells), Pv, and Sst interneurons in the somatosensory cortices of WT and *Stxbp1*^{tm1d/+} mice. (D) Summary data showing that the ratios of Pv and Sst interneurons to all somatosensory cortical neurons are similar between WT and *Stxbp1*^{tm1d/+} mice. The numbers and ages of mice are indicated in the figures. Each filled (male) or open (female) circle represents one mouse. Bar graphs are mean \pm s.e.m. n.s., $P > 0.05$.

Figure 8. Inhibitory synapses from Pv and Sst interneurons are differentially impaired in *Stxbp1*^{tm1d/+} mice.

(A) uIPSCs of a layer 2/3 pyramidal neuron ($V_m = +10$ mV) in the somatosensory cortex (upper panels) evoked by a train of 10-Hz action potentials in a nearby Pv interneuron (lower panels) from WT and *Stxbp1*^{tm1d/+} mice. 50 individual traces (lighter color) and the average trace (darker color) are superimposed. Note smaller uIPSCs in the *Stxbp1*^{tm1d/+} neuron. (B) Unitary connectivity rates from Pv interneurons to pyramidal neurons were similar between WT (27 connections out of 33 pairs) and *Stxbp1*^{tm1d/+} (26 connections out of 32 pairs) mice. (C) Cumulative frequencies of uIPSC amplitudes evoked by the first action potentials in the trains (median: WT, 217.3 pA; *Stxbp1*^{tm1d/+}, 127.1 pA). Inset, each filled (male) or open (female) circle

represents the uIPSC amplitude of one synaptic connection. **(D)** uIPSC amplitudes during the trains of action potentials were normalized by the amplitudes of the first uIPSCs. Note the similar synaptic depression between WT and *Stxbp1*^{tm1d/+} neurons. **(E–H)** Similar to (A–D), but for Sst interneurons. Unitary connectivity rates from Sst interneurons to pyramidal neurons (F) in *Stxbp1*^{tm1d/+} mice (25 connections out of 36 pairs) were less than WT mice (34 connections out of 36 pairs). The uIPSC amplitudes evoked by the first action potentials in the trains (G, median: 83.5 pA and 68.0 pA, respectively) and synaptic depression (H) were similar between WT and *Stxbp1*^{tm1d/+} mice. The ages of mice are indicated in the figures. Bar graphs are mean ± s.e.m. n.s., $P > 0.05$; *, $P < 0.05$; **, $P < 0.01$.

Figure 8-supplement 1. Intrinsic neuronal excitability of *Stxbp1*^{tm1d/+} mice is slightly increased.

(A) Membrane potentials (upper panels) in response to current injections (lower panels) in layer 2/3 pyramidal neurons of the somatosensory cortex from WT and *Stxbp1*^{tm1d/+} mice. **(B–D)** Summary data showing that *Stxbp1*^{tm1d/+} neurons had similar resting membrane potentials and rheobase currents as WT neurons, but their input resistances were 19% larger than WT neurons. The numbers and ages of recorded neurons are indicated in the figures. Each filled (male) or open (female) circle represents one neuron. Bar graphs are mean ± s.e.m. n.s., $P > 0.05$; *, $P < 0.05$.

Figure 8-supplement 2. Spontaneous excitatory inputs onto Pv and Sst interneurons are unaltered in *Stxbp1*^{tm1d/+} mice.

(A,B) sEPSCs of a Pv (A) or Sst (B) interneuron ($V_m = -70$ mV) in the layer 2/3 of the somatosensory cortex from WT or *Stxbp1^{tm1d/+}* mice. (C,D) Summary data showing that the frequency and amplitude of sEPSCs in Pv (C) and Sst (D) interneurons are similar between WT and *Stxbp1^{tm1d/+}* mice. The numbers and ages of recorded neurons are indicated in the figures. Each filled (male) or open (female) circle represents one neuron. Bar graphs are mean \pm s.e.m. n.s., $P > 0.05$.

Figure 9. Pv and Sst interneurons-mediated quantal IPSCs are isolated by a novel optogenetic method and are unaltered in *Stxbp1^{tm1d/+}* mice.

(A) Schematic of slice experiments in (B). ChR2 in Pv interneurons. (B) mIPSCs of a layer 2/3 pyramidal neuron ($V_m = +10$ mV) from the somatosensory cortex of WT or *Stxbp1^{tm1d/+}* mice. The intensity of blue light is indicated above the mIPSC traces. Note the increase of mIPSC frequency during blue light stimulation. The quantal IPSC trace was computed by subtracting the average mIPSC trace of the baseline period from that of the light stimulation period (bottom row). (C,D) As in (A,B), but for ChR2 in Sst interneurons. (E,F) Summary data showing that the average amplitude, charge, and decay time constant of Pv (E) or Sst (F) interneuron-mediated quantal IPSCs are similar between WT and *Stxbp1^{tm1d/+}* mice. The numbers and ages of recorded neurons are indicated in the figures. Each filled (male) or open (female) circle represents one neuron. Bar graphs are mean \pm s.e.m. n.s., $P > 0.05$.

Figure 9-supplement 1. Ramping down blue light intensity minimizes the tonic currents during optogenetic activation of interneurons.

1235 (A) Schematic of slice experiments in (B,C). ChR2 in Pv interneurons. (B,C) mIPSCs of the
1236 same layer 2/3 pyramidal neuron ($V_m = +10$ mV) from the somatosensory cortex of a WT mouse.
1237 The intensity of blue light is indicated above the mIPSC traces. Note the increase of tonic
1238 currents (i.e., the increase of holding currents) caused by the constant blue light stimulation (B),
1239 which was reduced by gradually decreasing the blue light intensity (C).

1240

1241 **Supplementary File 1. EEG phenotypes of individual WT and *Stxbp1*^{tm1d/+} mice.**

1242 The parameters characterizing the SWDs, myoclonic jerks, and myoclonic jumps of each WT and
1243 *Stxbp1*^{tm1d/+} mouse are presented in the table.

1244

1245 **Supplementary File 2. Phenotypic comparison of human patients and mouse models.**

1246 The phenotyping tests in mouse models (the second column) are grouped based on the clinical
1247 features of *STXBPI* encephalopathy (the first column). The results of phenotyping tests from
1248 different mouse models and studies are presented in the table.

1249

1250 **Supplementary File 3. Statistics of experimental results.**

1251 The details of all statistical tests, numbers of replicates, and *P* values are presented for each
1252 experiment in the table.

1253

1254 **Video 1. *Stxbp1*^{tm1d/+} mice show clusters of SWDs.**

1255 A representative video showing a SWD cluster in a *Stxbp1*^{tm1d/+} mouse. The top 3 traces are EEG
1256 signals from the left frontal cortex, right somatosensory cortex, and left somatosensory cortex.

1257 The bottom trace is the EMG signal from the neck muscle. The vertical line indicates the time of

1258 the current video frame. Note that the EEG signal from the left somatosensory cortex (the third
1259 channel) is inverted.

1260

1261 **Video 2. *Stxbp1*^{tm1d/+} mice show long SWDs.**

1262 A representative video showing a long SWD during REM sleep in a *Stxbp1*^{tm1d/+} mouse. The top
1263 3 traces are EEG signals from the left frontal cortex, right somatosensory cortex, and left
1264 somatosensory cortex. The bottom trace is the EMG signal from the neck muscle. The vertical
1265 line indicates the time of the current video frame. Note that the EEG signal from the left
1266 somatosensory cortex (the third channel) is inverted.

1267

1268 **Video 3. *Stxbp1*^{tm1d/+} mice show myoclonic jumps.**

1269 A representative video showing a myoclonic jump of a *Stxbp1*^{tm1d/+} mouse. The top 3 traces are
1270 EEG signals from the left frontal cortex, right somatosensory cortex, and left somatosensory
1271 cortex. The bottom trace is the EMG signal from the neck muscle. The vertical line indicates the
1272 time of the current video frame. Note that the EEG signal from the left somatosensory cortex (the
1273 third channel) is inverted.

1274

1275 **Video 4. *Stxbp1*^{tm1d/+} mice show myoclonic jerks.**

1276 A representative video showing a myoclonic jerk of a *Stxbp1*^{tm1d/+} mouse. The top 3 traces are
1277 EEG signals from the left frontal cortex, right somatosensory cortex, and left somatosensory
1278 cortex. The bottom trace is the EMG signal from the neck muscle. The vertical line indicates the
1279 time of the current video frame. Note that the EEG signal from the left somatosensory cortex (the
1280 third channel) is inverted.

1281 **References**

- 1282 Antunes M, Biala G (2012) The novel object recognition memory: neurobiology, test procedure,
1283 and its modifications. *Cogn Process* 13:93–110.
- 1284 Arain FM, Boyd KL, Gallagher MJ (2012) Decreased viability and absence-like epilepsy in mice
1285 lacking or deficient in the GABAA receptor $\alpha 1$ subunit. *Epilepsia* 53:e161–e165.
- 1286 Avanzini G, Shibasaki H, Rubboli G, Canafoglia L, Panzica F, Franceschetti S, Hallett M (2016)
1287 Neurophysiology of myoclonus and progressive myoclonus epilepsies. *Epileptic Disord*
1288 18:11–27.
- 1289 Baker K et al. (2018) SYT1-associated neurodevelopmental disorder: a case series. *Brain*
1290 141:2576–2591.
- 1291 Baker K, Gordon SL, Grozeva D, van Kogelenberg M, Roberts NY, Pike M, Blair E, Hurles ME,
1292 Chong WK, Baldeweg T, Kurian MA, Boyd SG, Cousin MA, Raymond FL (2015)
1293 Identification of a human synaptotagmin-1 mutation that perturbs synaptic vesicle cycling. *J*
1294 *Clin Invest* 125:1670–1678.
- 1295 Bayés À, van de Lagemaat LN, Collins MO, Croning MDR, Whittle IR, Choudhary JS, Grant
1296 SGN (2011) Characterization of the proteome, diseases and evolution of the human
1297 postsynaptic density. *Nat Neurosci* 14:19–21.
- 1298 Boutry-Kryza N, Labalme A, Ville D, de Bellescize J, Touraine R, Prieur F, Dimassi S, Poulat
1299 A-L, Till M, Rossi M, Bourel-Ponchel E, Delignières A, Le Moing A-G, Rivier C, Portes des
1300 V, Edery P, Calender A, Sanlaville D, Lesca G (2015) Molecular characterization of a cohort
1301 of 73 patients with infantile spasms syndrome. *Eur J Med Genet* 58:51–58.
- 1302 Boyden ES, Zhang F, Bamberg E, Nagel G, Deisseroth K (2005) Millisecond-timescale,
1303 genetically targeted optical control of neural activity. *Nat Neurosci* 8:1263–1268.
- 1304 Campbell IM et al. (2012) Novel 9q34.11 gene deletions encompassing combinations of four
1305 Mendelian disease genes: STXBP1, SPTAN1, ENG, and TOR1A. *Genet Med* 14:868–876.
- 1306 Carvill GL et al. (2013) Targeted resequencing in epileptic encephalopathies identifies de novo
1307 mutations in CHD2 and SYNGAP1. *Nat Genet* 45:825–830.
- 1308 Carvill GL et al. (2014) GABRA1 and STXBP1: novel genetic causes of Dravet syndrome.
1309 *Neurology* 82:1245–1253.
- 1310 Chang Y-F, Imam JS, Wilkinson MF (2007) The nonsense-mediated decay RNA surveillance
1311 pathway. *Annu Rev Biochem* 76:51–74.
- 1312 Cohen SJ, Stackman RW (2015) Assessing rodent hippocampal involvement in the novel object
1313 recognition task. A review. *Behav Brain Res* 285:105–117.
- 1314 Contestabile A, Magara S, Cancedda L (2017) The GABAergic Hypothesis for Cognitive

1315 Disabilities in Down Syndrome. *Front Cell Neurosci* 11:54.

1316 Deacon RMJ (2006) Digging and marble burying in mice: simple methods for in vivo
1317 identification of biological impacts. *Nat Protoc* 1:122–124.

1318 Deciphering Developmental Disorders Study (2015) Large-scale discovery of novel genetic
1319 causes of developmental disorders. *Nature* 519:223–228.

1320 Deciphering Developmental Disorders Study (2017) Prevalence and architecture of de novo
1321 mutations in developmental disorders. *Nature* 542:433–438.

1322 Depaulis A, Charpier S (2018) Pathophysiology of absence epilepsy: Insights from genetic
1323 models. *Neurosci Lett* 667:53–65.

1324 Deprez L, Weckhuysen S, Holmgren P, Suls A, Van Dyck T, Goossens D, Del-Favero J, Jansen
1325 A, Verhaert K, Lagae L, Jordanova A, Van Coster R, Yendle S, Berkovic SF, Scheffer I,
1326 Ceulemans B, De Jonghe P (2010) Clinical spectrum of early-onset epileptic
1327 encephalopathies associated with STXBP1 mutations. *Neurology* 75:1159–1165.

1328 Engel AG, Selcen D, Shen X-M, Milone M, Harper CM (2016) Loss of MUNC13-1 function
1329 causes microcephaly, cortical hyperexcitability, and fatal myasthenia. *Neurol Genet* 2:e105.

1330 Epi4K Consortium et al. (2013) De novo mutations in epileptic encephalopathies. *Nature*
1331 501:217–221.

1332 Fukuda H, Imagawa E, Hamanaka K, Fujita A, Mitsuhashi S, Miyatake S, Mizuguchi T, Takata
1333 A, Miyake N, Kramer U, Matsumoto N, Fattal-Valevski A (2018) A novel missense
1334 SNAP25b mutation in two affected siblings from an Israeli family showing seizures and
1335 cerebellar ataxia. *J Hum Genet* 63:673–676.

1336 Grone BP, Marchese M, Hamling KR, Kumar MG, Krasniak CS, Sicca F, Santorelli FM, Patel
1337 M, Baraban SC (2016) Epilepsy, Behavioral Abnormalities, and Physiological Comorbidities
1338 in Syntaxin-Binding Protein 1 (STXBP1) Mutant Zebrafish. *PLoS ONE* 11:e0151148.

1339 Guiberson NGL, Pineda A, Abramov D, Kharel P, Carnazza KE, Wragg RT, Dittman JS, Burré J
1340 (2018) Mechanism-based rescue of Munc18-1 dysfunction in varied encephalopathies by
1341 chemical chaperones. *Nature Communications* 9:3986.

1342 Hager T, Maroteaux G, Pont PD, Julsing J, van Vliet R, Stiedl O (2014) Munc18-1
1343 haploinsufficiency results in enhanced anxiety-like behavior as determined by heart rate
1344 responses in mice. *Behav Brain Res* 260:44–52.

1345 Hamada N, Iwamoto I, Tabata H, Nagata K-I (2017) MUNC18-1 gene abnormalities are
1346 involved in neurodevelopmental disorders through defective cortical architecture during
1347 brain development. *Acta Neuropathol Commun* 5:92–16.

1348 Hamdan FF et al. (2017) High Rate of Recurrent De Novo Mutations in Developmental and
1349 Epileptic Encephalopathies. *Am J Hum Genet* 101:664–685.

1350 Hamdan FF, Gauthier J, Dobrzeniecka S, Lortie A, Motttron L, Vanasse M, D'Anjou G, Lacaille
1351 JC, Rouleau GA, Michaud JL (2011) Intellectual disability without epilepsy associated with
1352 STXBP1 disruption. *Eur J Hum Genet* 19:607–609.

1353 Hamdan FF, Piton A, Gauthier J, Lortie A, Dubeau F, Dobrzeniecka S, Spiegelman D, Noreau A,
1354 Pellerin S, Côté M, Henrion E, Fombonne É, Motttron L, Marineau C, Drapeau P, Lafrenière
1355 RG, Lacaille JC, Rouleau GA, Michaud JL (2009) De novo STXBP1 mutations in mental
1356 retardation and nonsyndromic epilepsy. *Ann Neurol* 65:748–753.

1357 Harrison SD, Broadie K, van de Goor J, Rubin GM (1994) Mutations in the *Drosophila* Rop
1358 gene suggest a function in general secretion and synaptic transmission. *Neuron* 13:555–566.

1359 Hayashi S, Lewis P, Pevny L, McMahon AP (2002) Efficient gene modulation in mouse epiblast
1360 using a Sox2Cre transgenic mouse strain. *Mech Dev* 119 Suppl 1:S97–S101.

1361 Heeroma JH, Roelandse M, Wierda K, van Aerde KI, Toonen RFG, Hensbroek RA, Brussaard A,
1362 Matus A, Verhage M (2004) Trophic support delays but does not prevent cell-intrinsic
1363 degeneration of neurons deficient for munc18-1. *The European journal of neuroscience*
1364 20:623–634.

1365 Hippenmeyer S, Vrieseling E, Sigrist M, Portmann T, Laengle C, Ladle DR, Arber S (2005) A
1366 developmental switch in the response of DRG neurons to ETS transcription factor signaling.
1367 *PLoS Biol* 3:e159.

1368 Hoischen A, Krumm N, Eichler EE (2014) Prioritization of neurodevelopmental disease genes
1369 by discovery of new mutations. *Nat Neurosci* 17:764–772.

1370 Ito-Ishida A, Ure K, Chen H, Swann JW, Zoghbi HY (2015) Loss of MeCP2 in Parvalbumin-and
1371 Somatostatin-Expressing Neurons in Mice Leads to Distinct Rett Syndrome-like Phenotypes.
1372 *Neuron* 88:651–658.

1373 Kovačević J, Maroteaux G, Schut D, Loos M, Dubey M, Pitsch J, Remmelink E, Koopmans B,
1374 Crowley J, Cornelisse LN, Sullivan PF, Schoch S, Toonen RF, Stiedl O, Verhage M (2018)
1375 Protein instability, haploinsufficiency, and cortical hyper-excitability underlie STXBP1
1376 encephalopathy. *Brain* 141:1350–1374.

1377 Kraushaar U, Jonas P (2000) Efficacy and stability of quantal GABA release at a hippocampal
1378 interneuron-principal neuron synapse. *J Neurosci* 20:5594–5607.

1379 Law C, Schaan Profes M, Levesque M, Kaltschmidt JA, Verhage M, Kania A (2016) Normal
1380 Molecular Specification and Neurodegenerative Disease-Like Death of Spinal Neurons
1381 Lacking the SNARE-Associated Synaptic Protein Munc18-1. *Journal of Neuroscience*
1382 36:561–576.

1383 Lee E, Lee J, Kim E (2017) Excitation/Inhibition Imbalance in Animal Models of Autism
1384 Spectrum Disorders. *Biol Psychiatry* 81:838–847.

1385 Letts VA, Beyer BJ, Frankel WN (2014) Hidden in plain sight: spike-wave discharges in mouse

1386 inbred strains. *Genes Brain Behav* 13:519–526.

1387 Li X, Gutierrez DV, Hanson MG, Han J, Mark MD, Chiel H, Hegemann P, Landmesser LT,
 1388 Herlitze S (2005) Fast noninvasive activation and inhibition of neural and network activity
 1389 by vertebrate rhodopsin and green algae channelrhodopsin. *Proc Natl Acad Sci USA*
 1390 102:17816–17821.

1391 Lindy AS, Stosser MB, Butler E, Downtain-Pickersgill C, Shanmugham A, Retterer K, Brandt T,
 1392 Richard G, McKnight DA (2018) Diagnostic outcomes for genetic testing of 70 genes in
 1393 8565 patients with epilepsy and neurodevelopmental disorders. *Epilepsia* 59:1062–1071.

1394 Lipstein N et al. (2017) Synaptic UNC13A protein variant causes increased neurotransmission
 1395 and dyskinetic movement disorder. *J Clin Invest* 127:1005–1018.

1396 Luthi A, Di Paolo G, Cremona O, Daniell L, De Camilli P, McCormick DA (2001) Synaptotagmin
 1397 1 contributes to maintaining the stability of GABAergic transmission in primary cultures of
 1398 cortical neurons. *J Neurosci* 21:9101–9111.

1399 Madisen L, Zwingman TA, Sunken SM, Oh SW, Zariwala HA, Gu H, Ng LL, Palmiter RD,
 1400 Hawrylycz MJ, Jones AR, Lein ES, Zeng H (2010) A robust and high-throughput Cre
 1401 reporting and characterization system for the whole mouse brain. *Nat Neurosci* 13:133–140.

1402 Maheshwari A, Noebels JL (2014) Monogenic models of absence epilepsy: windows into the
 1403 complex balance between inhibition and excitation in thalamocortical microcircuits. *Progress*
 1404 *in Brain Research* 213:223–252.

1405 Marín O (2012) Interneuron dysfunction in psychiatric disorders. *Nat Rev Neurosci* 13:107–120.

1406 Messier JE, Chen H, Cai Z-L, Xue M (2018) Targeting light-gated chloride channels to neuronal
 1407 somatodendritic domain reduces their excitatory effect in the axon. *Elife* 7:232.

1408 Mignot C, Moutard M-L, Trouillard O, Gourfinkel-An I, Jacquette A, Arveiler B, Morice-Picard
 1409 F, Lacombe D, Chiron C, Ville D, Charles P, Leguern E, Depienne C, Héron D (2011)
 1410 STXBP1-related encephalopathy presenting as infantile spasms and generalized tremor in
 1411 three patients. *Epilepsia* 52:1820–1827.

1412 Milh M, Villeneuve N, Chouchane M, Kaminska A, Laroche C, Barthez MA, Gitiaux C, Bartoli
 1413 C, Borges-Correia A, Cacciagli P, Mignon-Ravix C, Cuberos H, Chabrol B, Villard L (2011)
 1414 Epileptic and nonepileptic features in patients with early onset epileptic encephalopathy and
 1415 STXBP1 mutations. *Epilepsia* 52:1828–1834.

1416 Miyamoto H, Shimohata A, Abe M, Abe T, Mazaki E, Amano K, Suzuki T, Tatsukawa T,
 1417 Itohara S, Sakimura K, Yamakawa K (2017) Potentiation of excitatory synaptic transmission
 1418 ameliorates aggression in mice with Stxbp1 haploinsufficiency. *Hum Mol Genet* 26:4961–
 1419 4974.

1420 Miyamoto H, Tatsukawa T, Shimohata A, Yamagata T, Suzuki T, Amano K, Mazaki E, Raveau
 1421 M, Ogiwara I, Oba-Asaka A, Hensch TK, Itohara S, Sakimura K, Kobayashi K, Kobayashi

- 1422 K, Yamakawa K (2019) Impaired cortico-striatal excitatory transmission triggers epilepsy.
1423 Nature Communications 10:1917.
- 1424 Nagel G, Szellas T, Huhn W, Kateriya S, Adeishvili N, Berthold P, Ollig D, Hegemann P,
1425 Bamberg E (2003) Channelrhodopsin-2, a directly light-gated cation-selective membrane
1426 channel. Proc Natl Acad Sci USA 100:13940–13945.
- 1427 Nelson SB, Valakh V (2015) Excitatory/Inhibitory Balance and Circuit Homeostasis in Autism
1428 Spectrum Disorders. Neuron 87:684–698.
- 1429 Ogden KK, Ozkan ED, Rumbaugh G (2016) Prioritizing the development of mouse models for
1430 childhood brain disorders. Neuropharmacology 100:2–16.
- 1431 Orock A, Logan S, Deák F (2018) Munc18-1 haploinsufficiency impairs learning and memory
1432 by reduced synaptic vesicular release in a model of Ohtahara syndrome. Mol Cell Neurosci
1433 88:33–42.
- 1434 Otsuka M, Oguni H, Liang J-S, Ikeda H, Imai K, Hirasawa K, Imai K, Tachikawa E, Shimojima
1435 K, Osawa M, Yamamoto T (2010) STXBP1 mutations cause not only Ohtahara syndrome
1436 but also West syndrome--result of Japanese cohort study. Epilepsia 51:2449–2452.
- 1437 Patzke C, Han Y, Covy J, Yi F, Maxeiner S, Wernig M, Südhof TC (2015) Analysis of
1438 conditional heterozygous STXBP1 mutations in human neurons. J Clin Invest 125:3560–
1439 3571.
- 1440 Paz JT, Huguenard JR (2015) Microcircuits and their interactions in epilepsy: is the focus out of
1441 focus? Nat Neurosci 18:351–359.
- 1442 Prakash R, Yizhar O, Grewe B, Ramakrishnan C, Wang N, Goshen I, Packer AM, Peterka DS,
1443 Yuste R, Schnitzer MJ, Deisseroth K (2012) Two-photon optogenetic toolbox for fast
1444 inhibition, excitation and bistable modulation. Nature Publishing Group 9:1171–1179.
- 1445 Ramamoorthi K, Lin Y (2011) The contribution of GABAergic dysfunction to
1446 neurodevelopmental disorders. Trends Mol Med 17:452–462.
- 1447 Rauch A et al. (2012) Range of genetic mutations associated with severe non-syndromic sporadic
1448 intellectual disability: an exome sequencing study. Lancet 380:1674–1682.
- 1449 Raymond CS, Soriano P (2007) High-efficiency FLP and PhiC31 site-specific recombination in
1450 mammalian cells. PLoS ONE 2:e162.
- 1451 Rizo J, Xu J (2015) The Synaptic Vesicle Release Machinery. Annu Rev Biophys 44:339–367.
- 1452 Rohena L, Neidich J, Truitt Cho M, Gonzalez KD, Tang S, Devinsky O, Chung WK (2013)
1453 Mutation in SNAP25 as a novel genetic cause of epilepsy and intellectual disability. Rare
1454 Dis 1:e26314.
- 1455 Rubinstein M, Han S, Tai C, Westenbroek RE, Hunker A, Scheuer T, Catterall WA (2015)

1456 Dissecting the phenotypes of Dravet syndrome by gene deletion. *Brain* 138:2219–2233.

1457 Saitsu H et al. (2010) STXBP1 mutations in early infantile epileptic encephalopathy with
1458 suppression-burst pattern. *Epilepsia* 51:2397–2405.

1459 Saitsu H, Kato M, Mizuguchi T, Hamada K, Osaka H, Tohyama J, Uruno K, Kumada S,
1460 Nishiyama K, Nishimura A, Okada I, Yoshimura Y, Hirai S-I, Kumada T, Hayasaka K,
1461 Fukuda A, Ogata K, Matsumoto N (2008) De novo mutations in the gene encoding STXBP1
1462 (MUNC18-1) cause early infantile epileptic encephalopathy. *Nat Genet* 40:782–788.

1463 Salpietro V et al. (2019) Mutations in the Neuronal Vesicular SNARE VAMP2 Affect Synaptic
1464 Membrane Fusion and Impair Human Neurodevelopment. *Am J Hum Genet* 104:721–730.

1465 Schubert J et al. (2014) Mutations in STX1B, encoding a presynaptic protein, cause fever-
1466 associated epilepsy syndromes. *Nat Genet* 46:1327–1332.

1467 Shen X-M, Selcen D, Brengman J, Engel AG (2014) Mutant SNAP25B causes myasthenia,
1468 cortical hyperexcitability, ataxia, and intellectual disability. *Neurology* 83:2247–2255.

1469 Skarnes WC, Rosen B, West AP, Koutsourakis M, Bushell W, Iyer V, Mujica AO, Thomas M,
1470 Harrow J, Cox T, Jackson D, Severin J, Biggs P, Fu J, Nefedov M, de Jong PJ, Stewart AF,
1471 Bradley A (2011) A conditional knockout resource for the genome-wide study of mouse
1472 gene function. *Nature* 474:337–342.

1473 Stamberger H et al. (2016) STXBP1 encephalopathy: A neurodevelopmental disorder including
1474 epilepsy. *Neurology* 86:954–962.

1475 Stessman HAF et al. (2017) Targeted sequencing identifies 91 neurodevelopmental-disorder risk
1476 genes with autism and developmental-disability biases. *Nat Genet* 49:515–526.

1477 Suri M, Evers JMG, Laskowski RA, O'Brien S, Baker K, Clayton-Smith J, Dabir T, Josifova D,
1478 Joss S, Kerr B, Kraus A, McEntagart M, Morton J, Smith A, Splitt M, Thornton JM, DDD
1479 Study, Wright CF (2017) Protein structure and phenotypic analysis of pathogenic and
1480 population missense variants in STXBP1. *Mol Genet Genomic Med* 5:495–507.

1481 Taniguchi H, He M, Wu P, Kim S, Paik R, Sugino K, Kvitsiani D, Kvitsani D, Fu Y, Lu J, Lin Y,
1482 Miyoshi G, Shima Y, Fishell G, Nelson SB, Huang ZJ (2011) A resource of Cre driver lines
1483 for genetic targeting of GABAergic neurons in cerebral cortex. *Neuron* 71:995–1013.

1484 Testa G, Schaft J, Van Der Hoeven F, Glaser S, Anastassiadis K, Zhang Y, Hermann T,
1485 Stremmel W, Stewart AF (2004) A reliable lacZ expression reporter cassette for
1486 multipurpose, knockout-first alleles. *genesis* 38:151–158.

1487 Thomas A, Burant A, Bui N, Graham D, Yuva-Paylor LA, Paylor R (2009) Marble burying
1488 reflects a repetitive and perseverative behavior more than novelty-induced anxiety.
1489 *Psychopharmacology (Berl)* 204:361–373.

1490 Toonen RFG, Wierda K, Sons MS, de Wit H, Cornelisse LN, Brussaard A, Plomp JJ, Verhage M

1491 (2006) Munc18-1 expression levels control synapse recovery by regulating readily releasable
1492 pool size. *Proc Natl Acad Sci USA* 103:18332–18337.

1493 Varoqueaux F, Sigler A, Rhee J-S, Brose N, Enk C, Reim K, Rosenmund C (2002) Total arrest
1494 of spontaneous and evoked synaptic transmission but normal synaptogenesis in the absence
1495 of Munc13-mediated vesicle priming. *Proc Natl Acad Sci USA* 99:9037–9042.

1496 Verhage M, Maia AS, Plomp JJ, Brussaard AB, Heeroma JH, Vermeer H, Toonen RF, Hammer
1497 RE, van den Berg TK, Missler M, Geuze HJ, Sudhof TC (2000) Synaptic assembly of the
1498 brain in the absence of neurotransmitter secretion. *Science* 287:864–869.

1499 Weckhuysen S et al. (2013) Reduction of seizure frequency after epilepsy surgery in a patient
1500 with STXBP1 encephalopathy and clinical description of six novel mutation carriers.
1501 *Epilepsia* 54:e74–e80.

1502 Weimer RM, Richmond JE, Davis WS, Hadwiger G, Nonet ML, Jorgensen EM (2003) Defects
1503 in synaptic vesicle docking in unc-18 mutants. *Nat Neurosci* 6:1023–1030.

1504 Wolking S et al. (2019) Clinical spectrum of STX1B-related epileptic disorders. *Neurology*
1505 92:e1238–e1249.

1506 Wolmarans DW, Stein DJ, Harvey BH (2016) Of mice and marbles: Novel perspectives on
1507 burying behavior as a screening test for psychiatric illness. *Cogn Affect Behav Neurosci*
1508 16:551–560.

1509 Wu MN, Littleton JT, Bhat MA, Prokop A, Bellen HJ (1998) ROP, the *Drosophila* Sec1
1510 homolog, interacts with syntaxin and regulates neurotransmitter release in a dosage-
1511 dependent manner. *EMBO J* 17:127–139.

1512 Xue M, Atallah BV, Scanziani M (2014) Equalizing excitation-inhibition ratios across visual
1513 cortical neurons. *Nature* 511:596–600.

1514 Zhu X, Need AC, Petrovski S, Goldstein DB (2014) One gene, many neuropsychiatric disorders:
1515 lessons from Mendelian diseases. *Nat Neurosci* 17:773–781.

1516

Figure 1

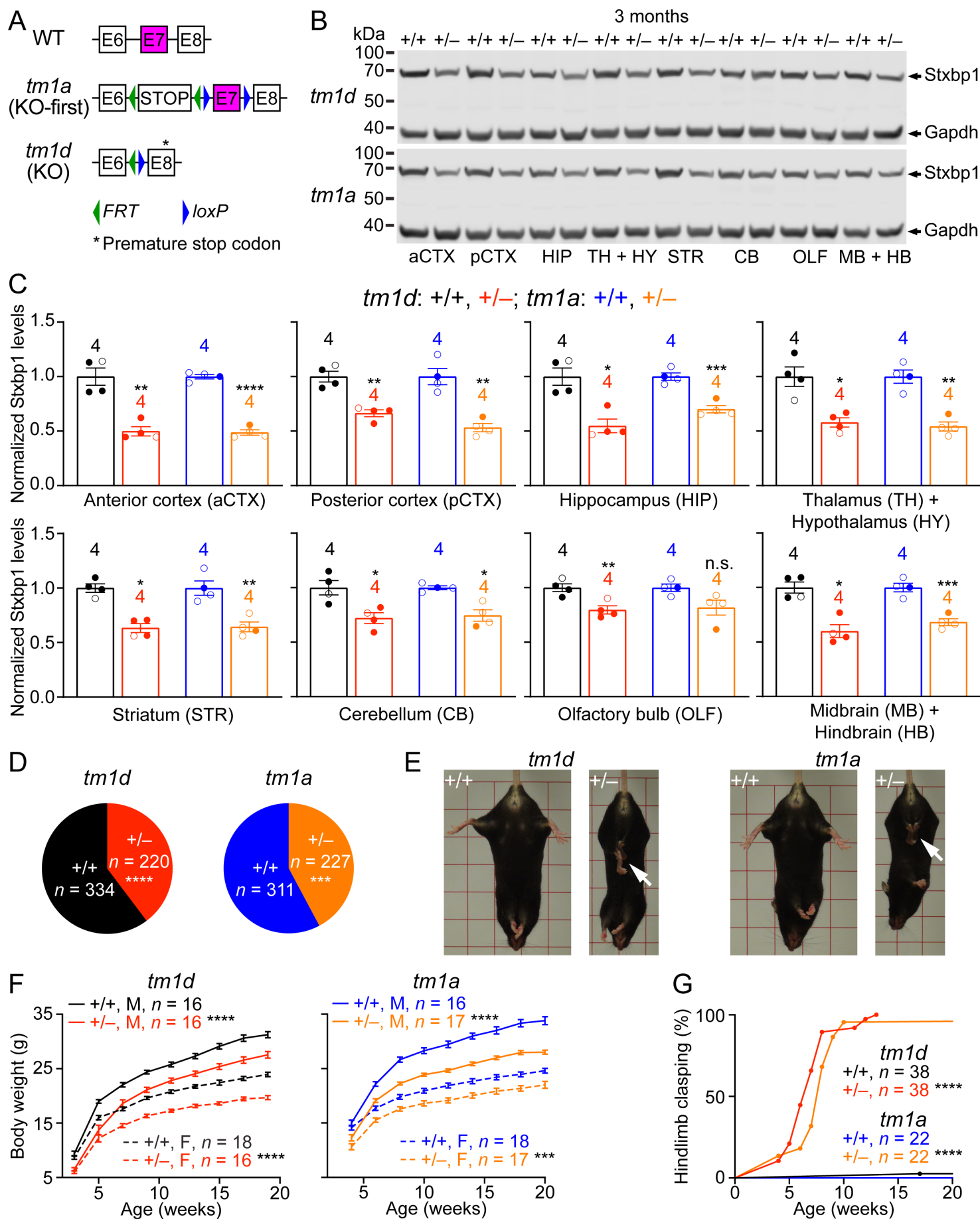


Figure 1-supplement 1

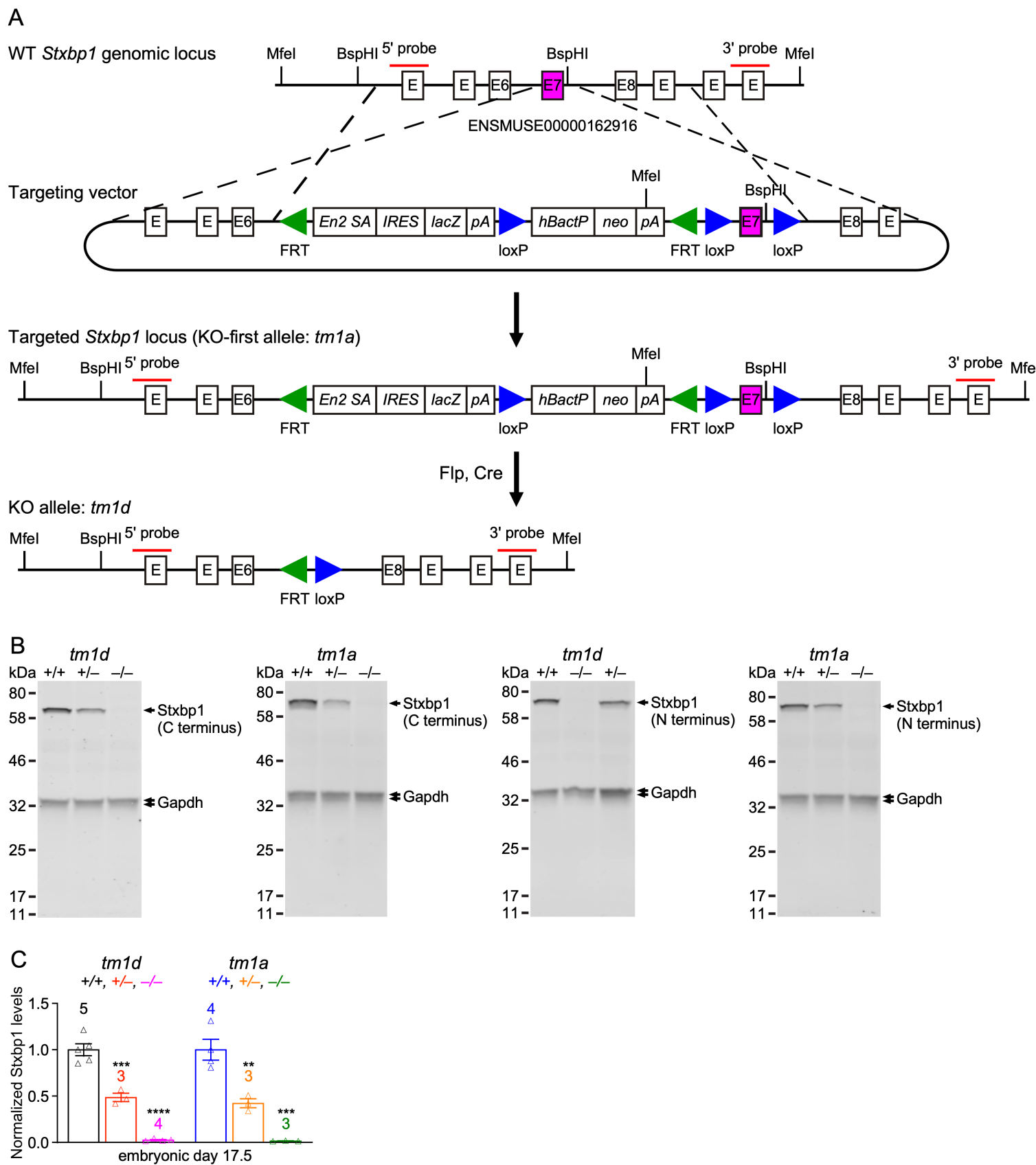


Figure 1-supplement 2

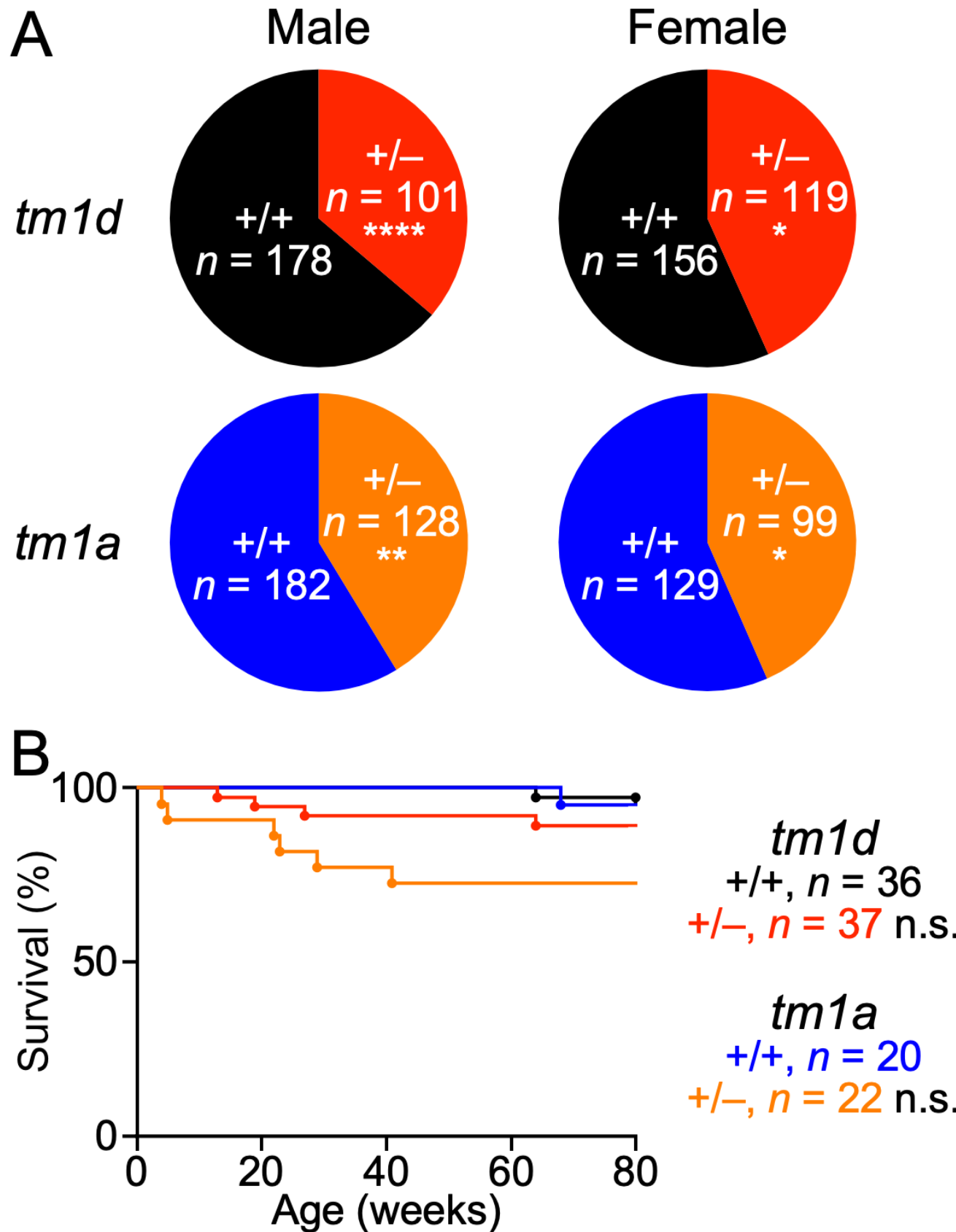


Figure 2

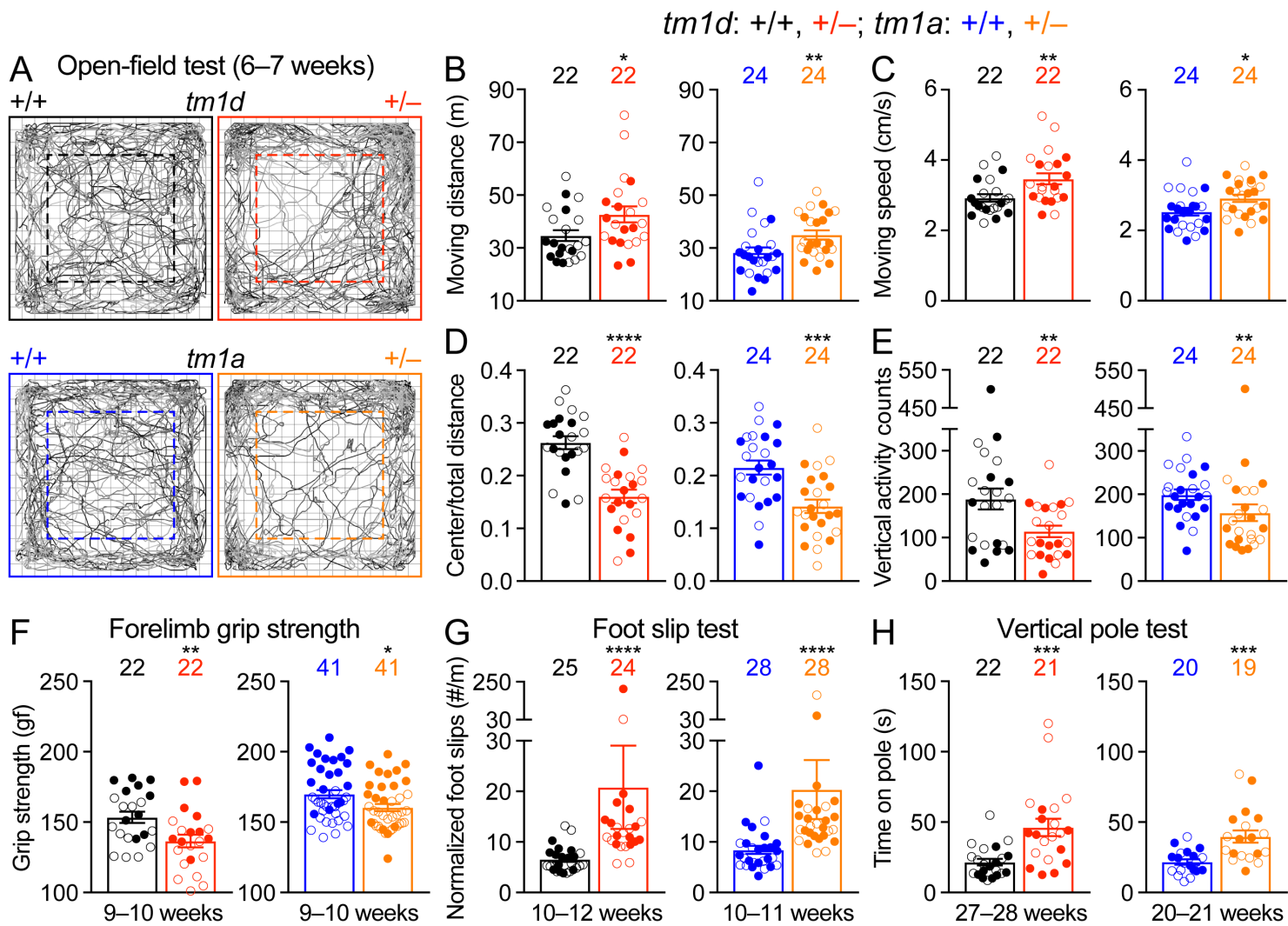


Figure 2-supplement 1

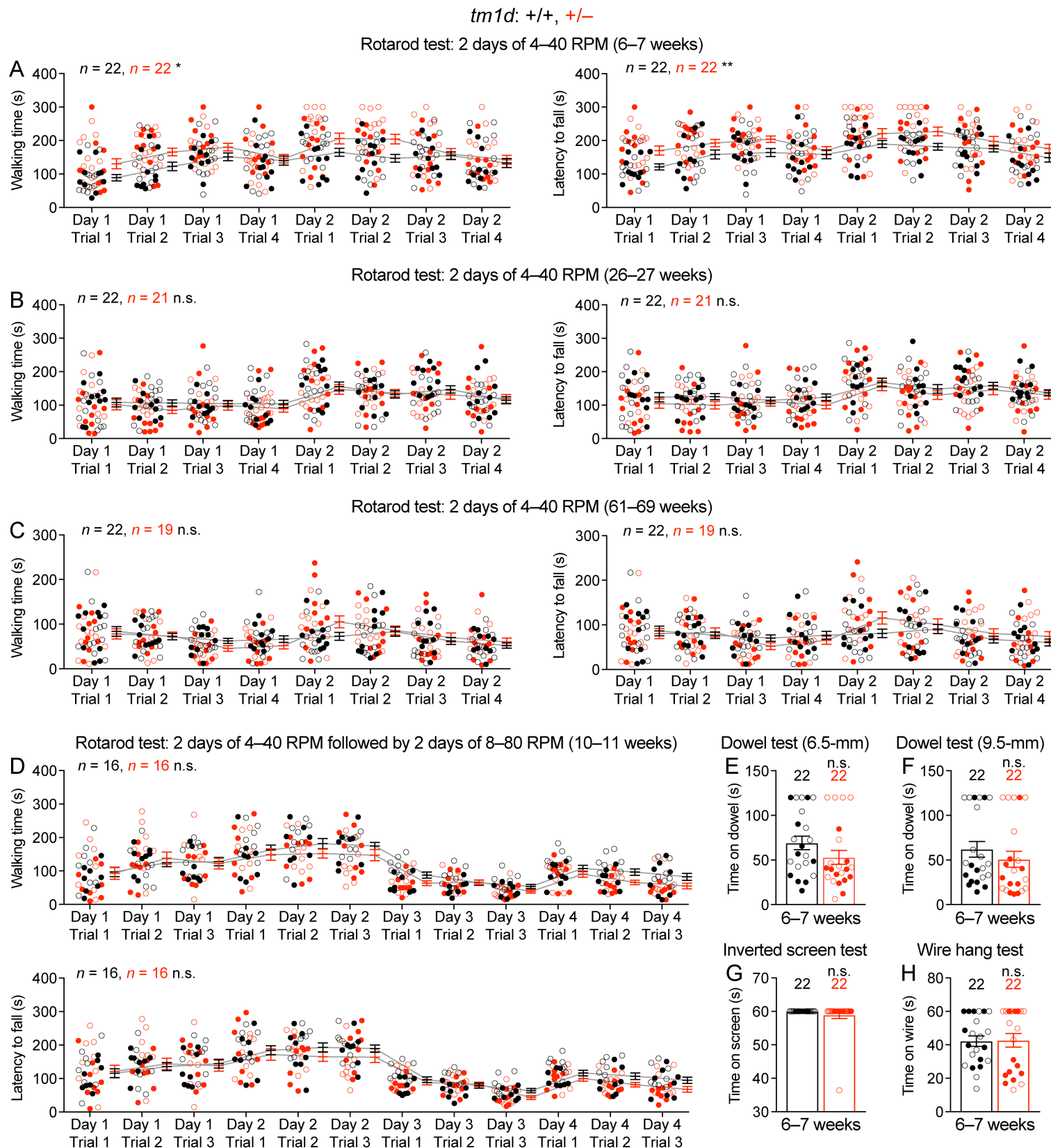


Figure 2-supplement 2

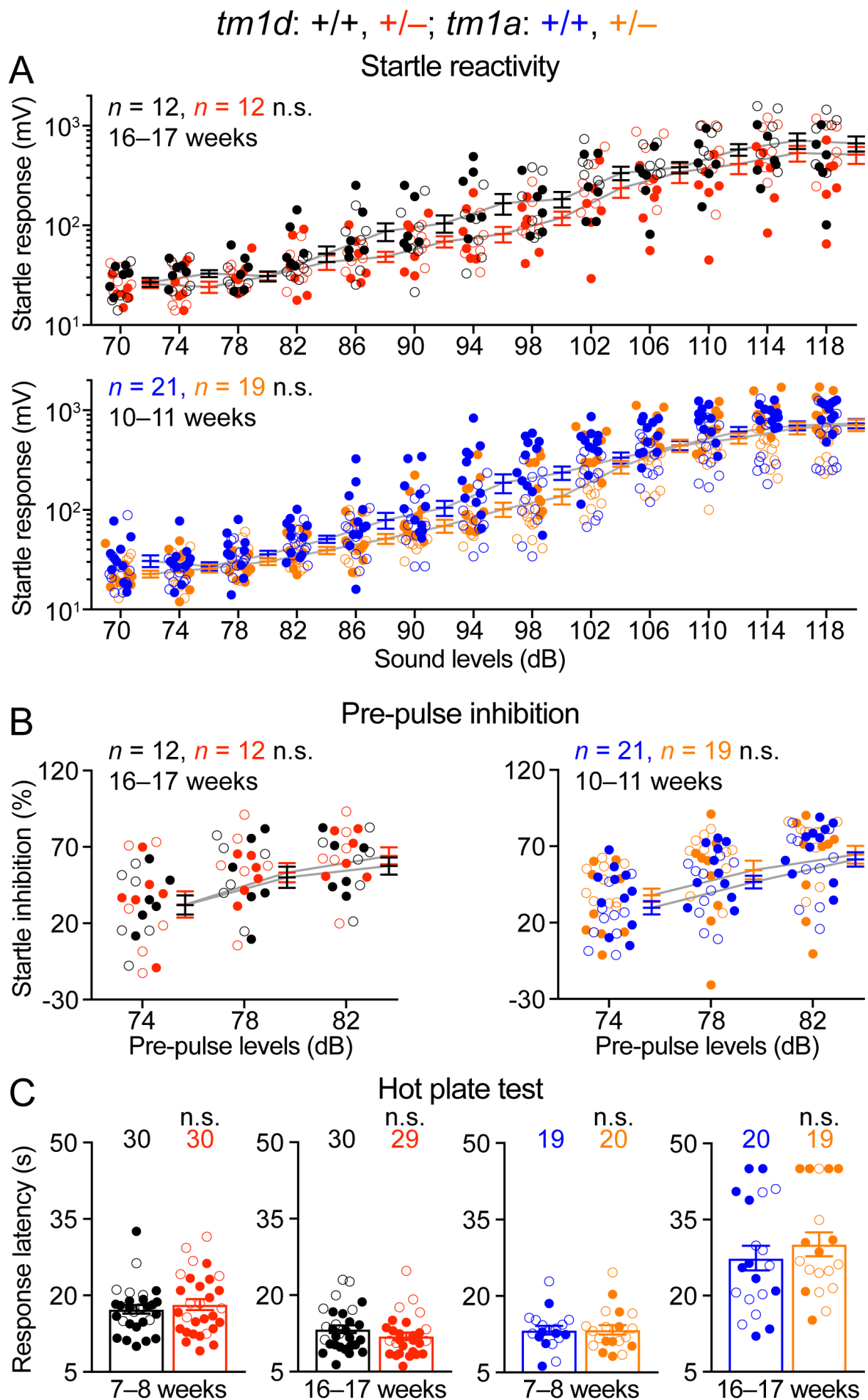


Figure 3

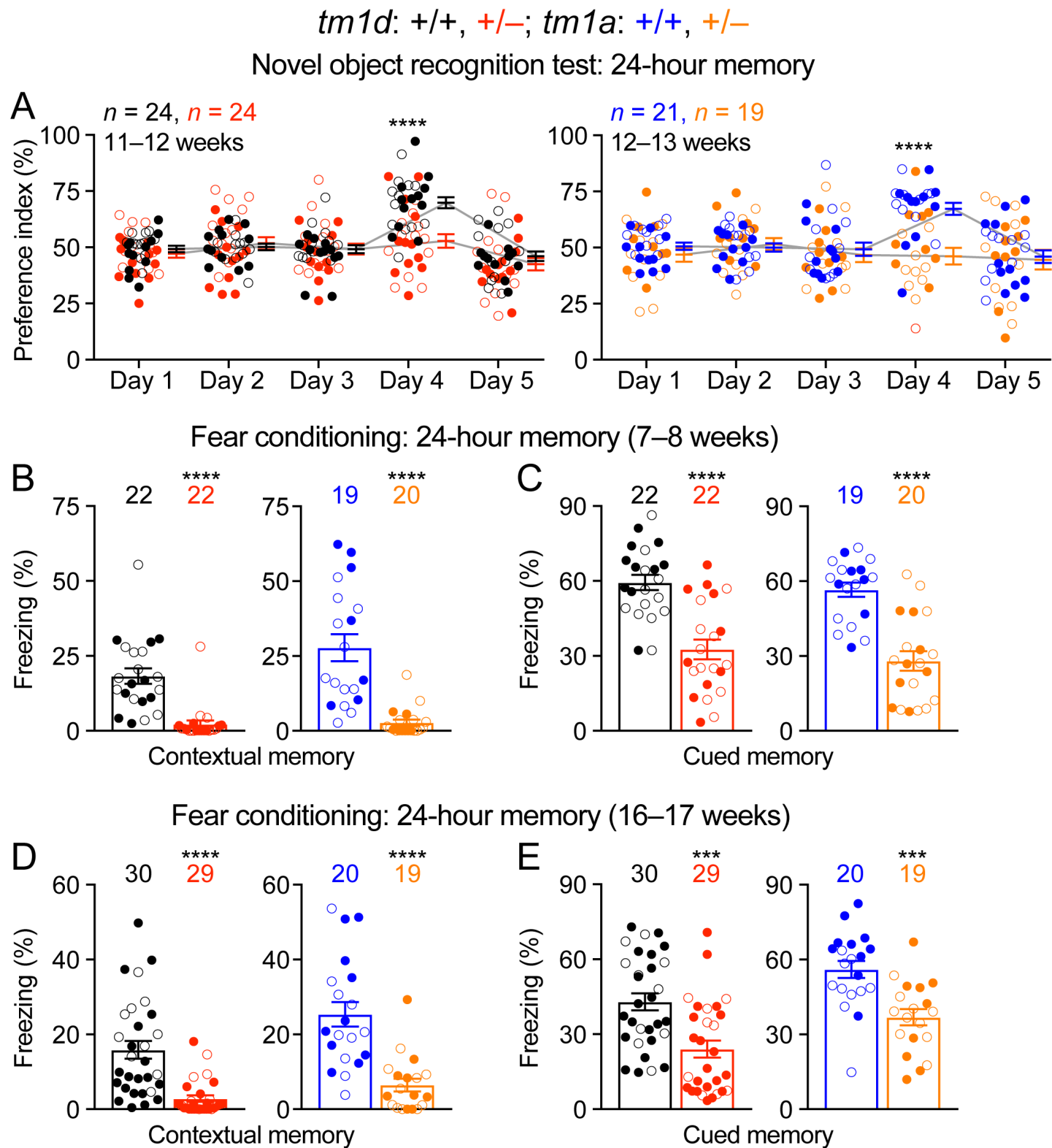


Figure 3-supplement 1

tm1d: +/+, +/-; *tm1a*: +/+, +/-

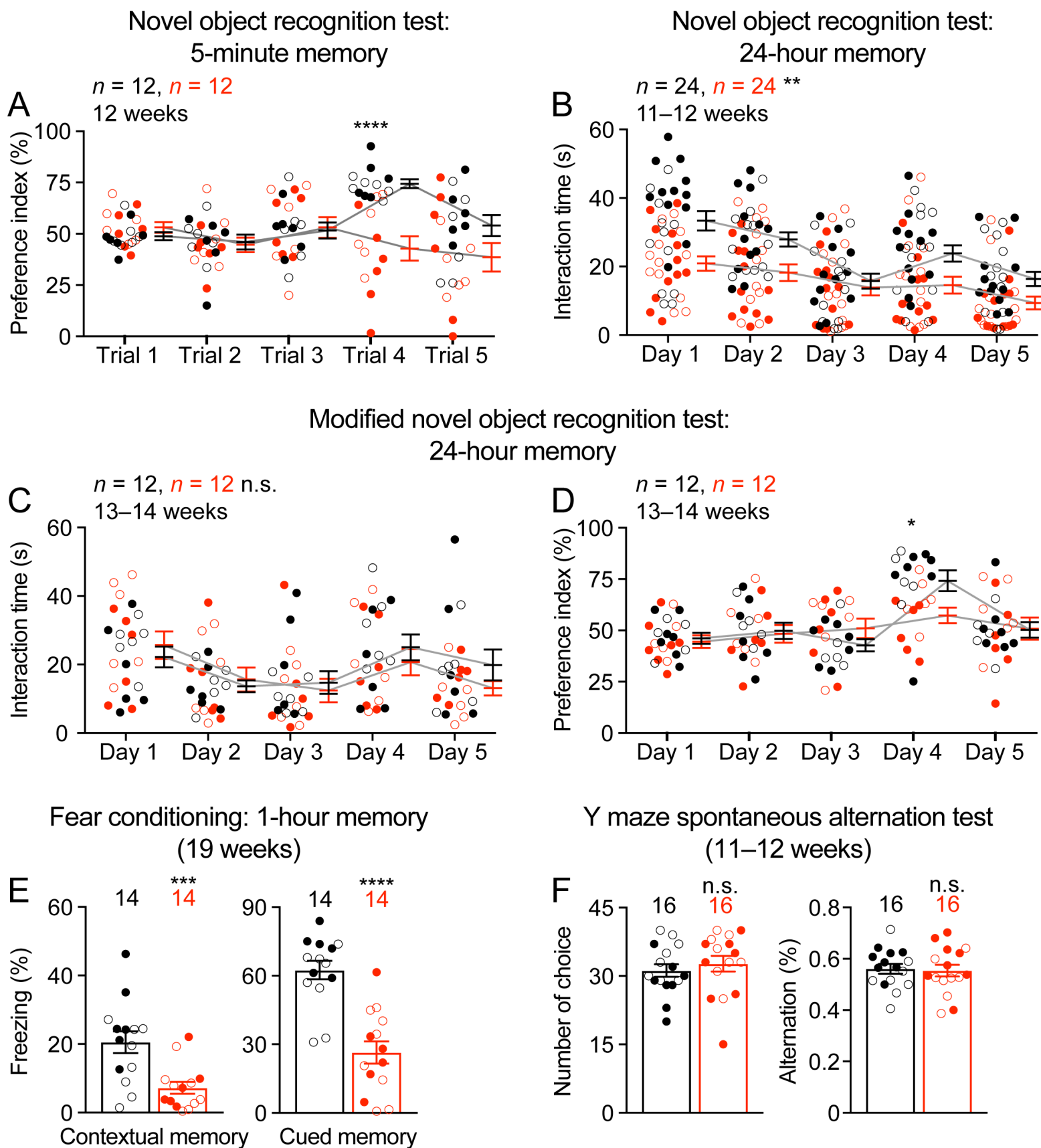
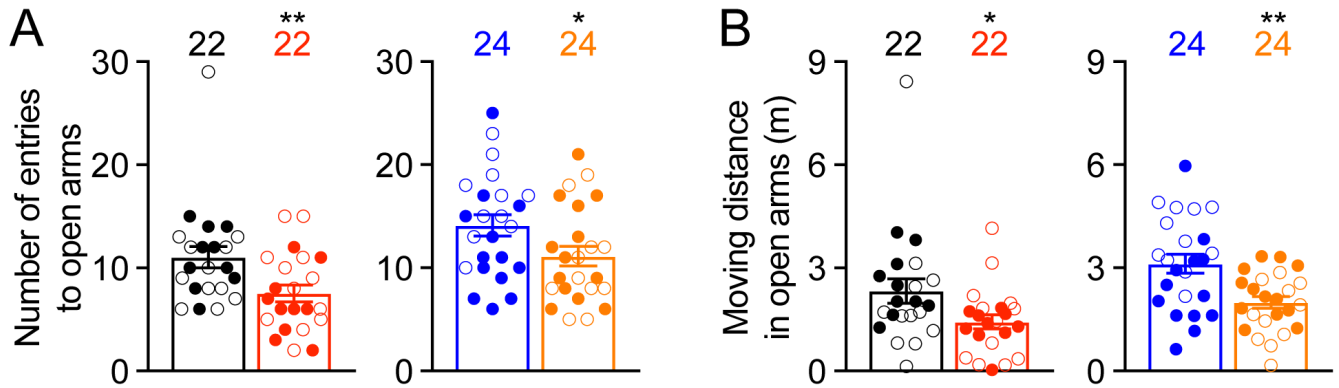


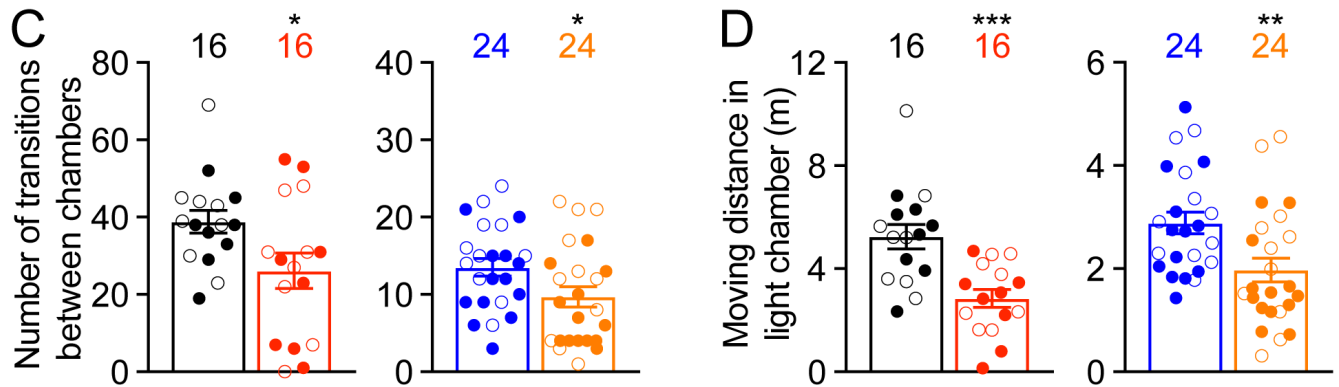
Figure 4

tm1d: +/+, +/-; *tm1a*: +/+, +/-

Elevated plus maze test (6 weeks)



Light-dark chamber test (9–10 weeks)



Hole-board test (9–10 weeks)

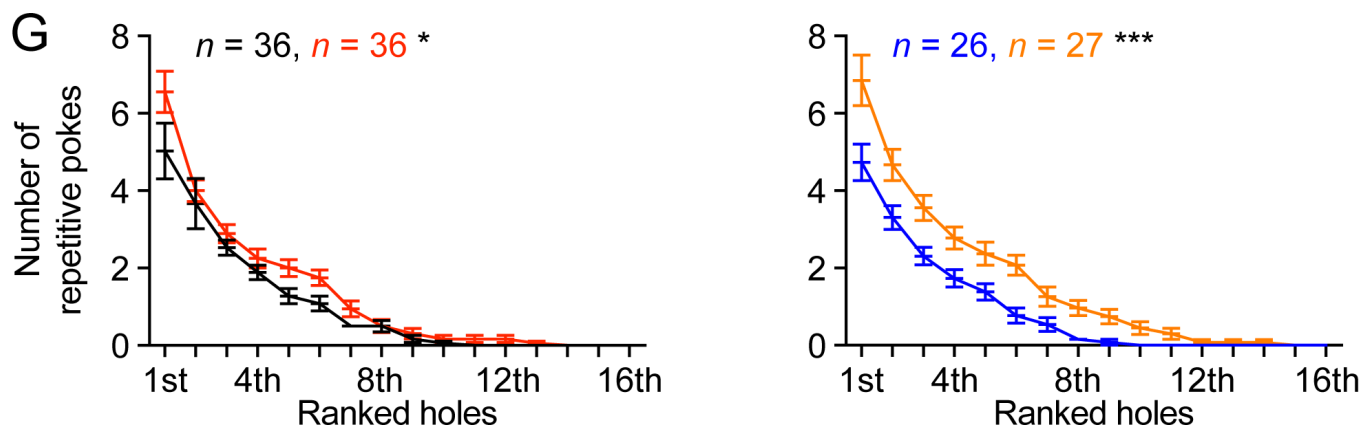
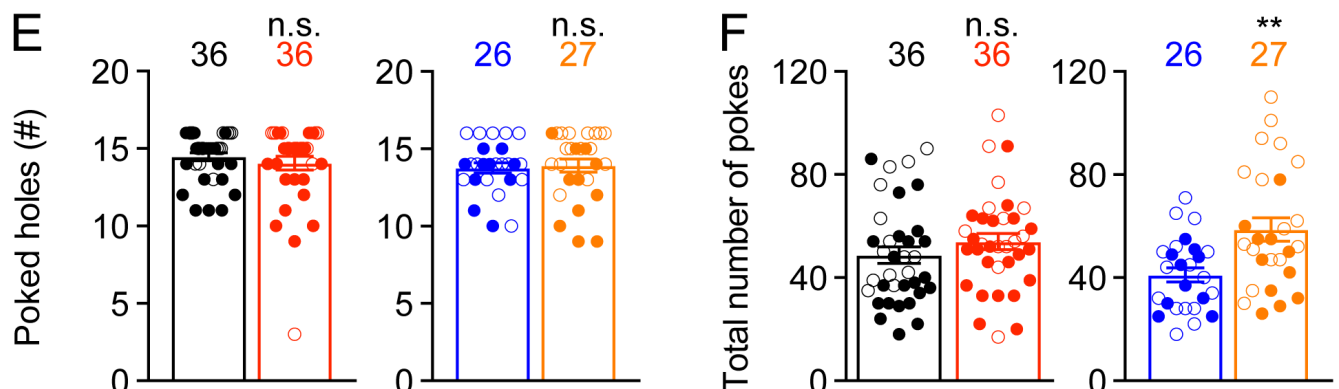


Figure 4-supplement 1

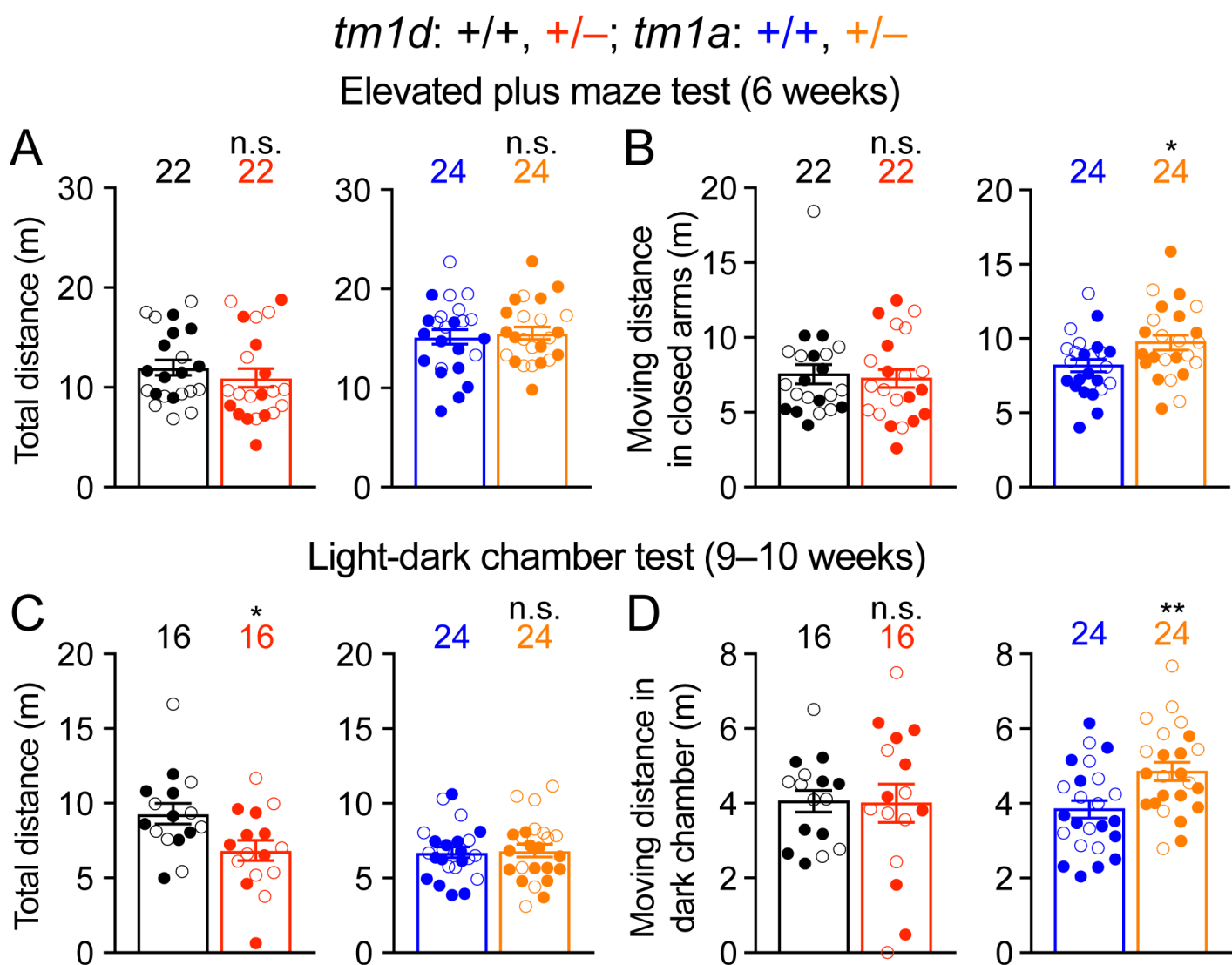


Figure 5

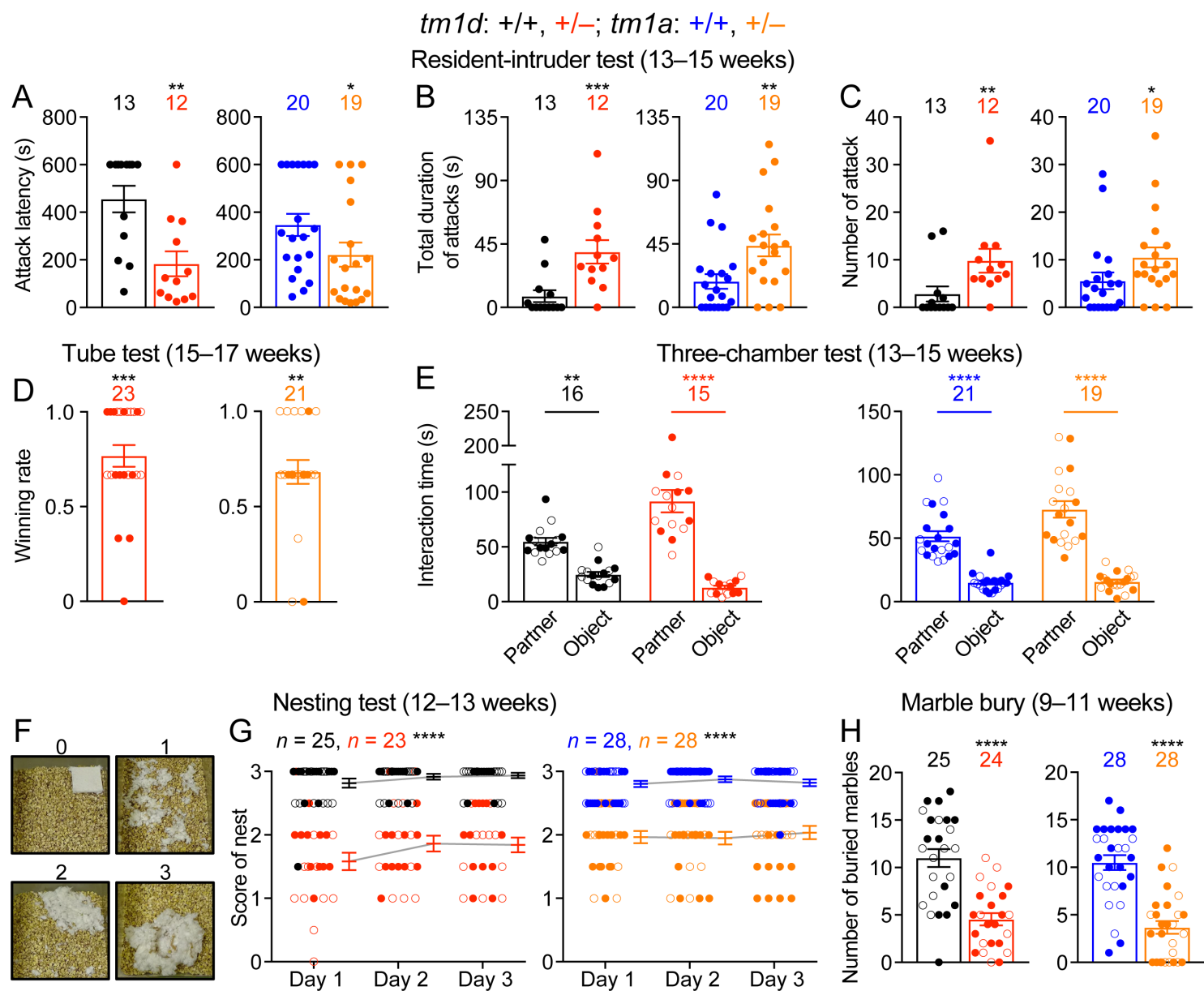


Figure 5-supplement 1

tm1d: $+/+$, $+/-$

Partition test (13–14 weeks)

A

$n = 16$, $n = 16$ n.s.

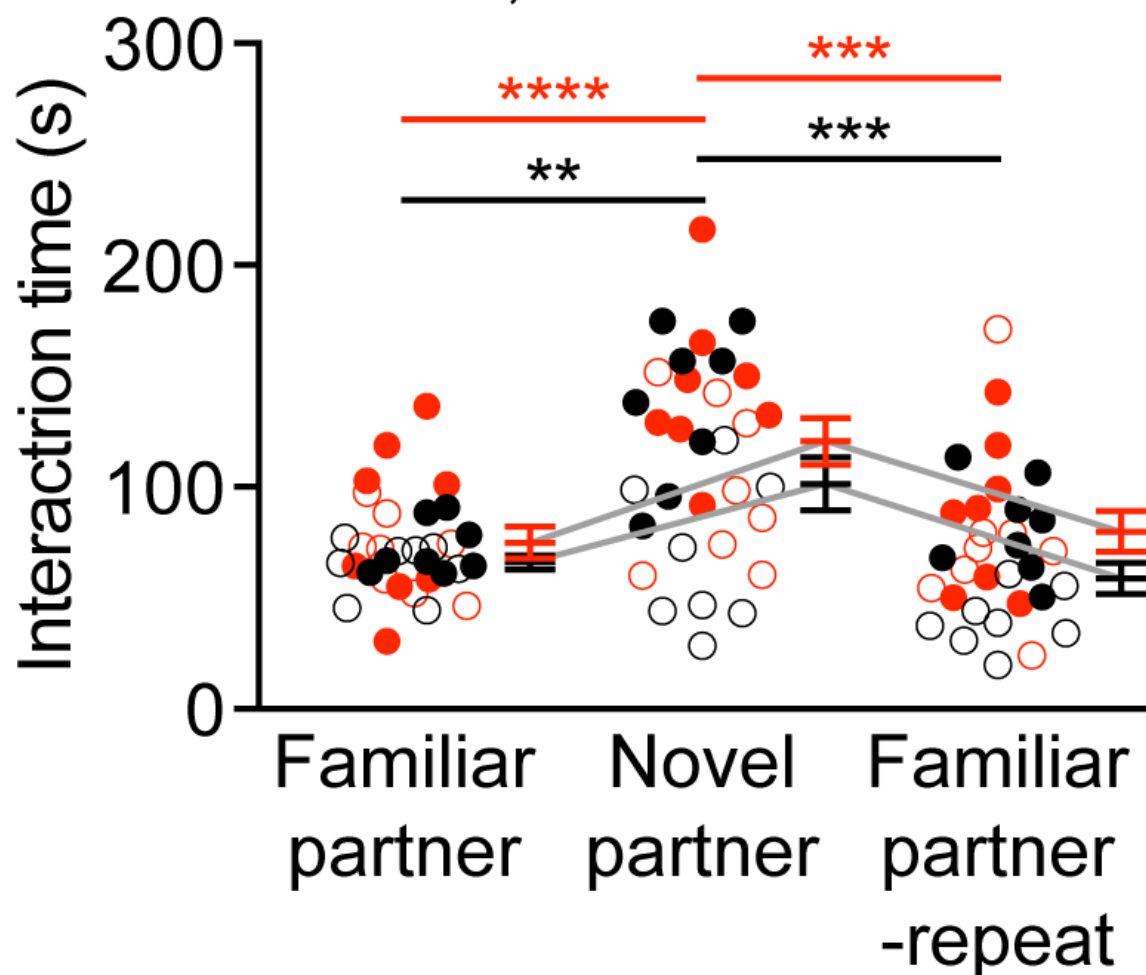


Figure 6

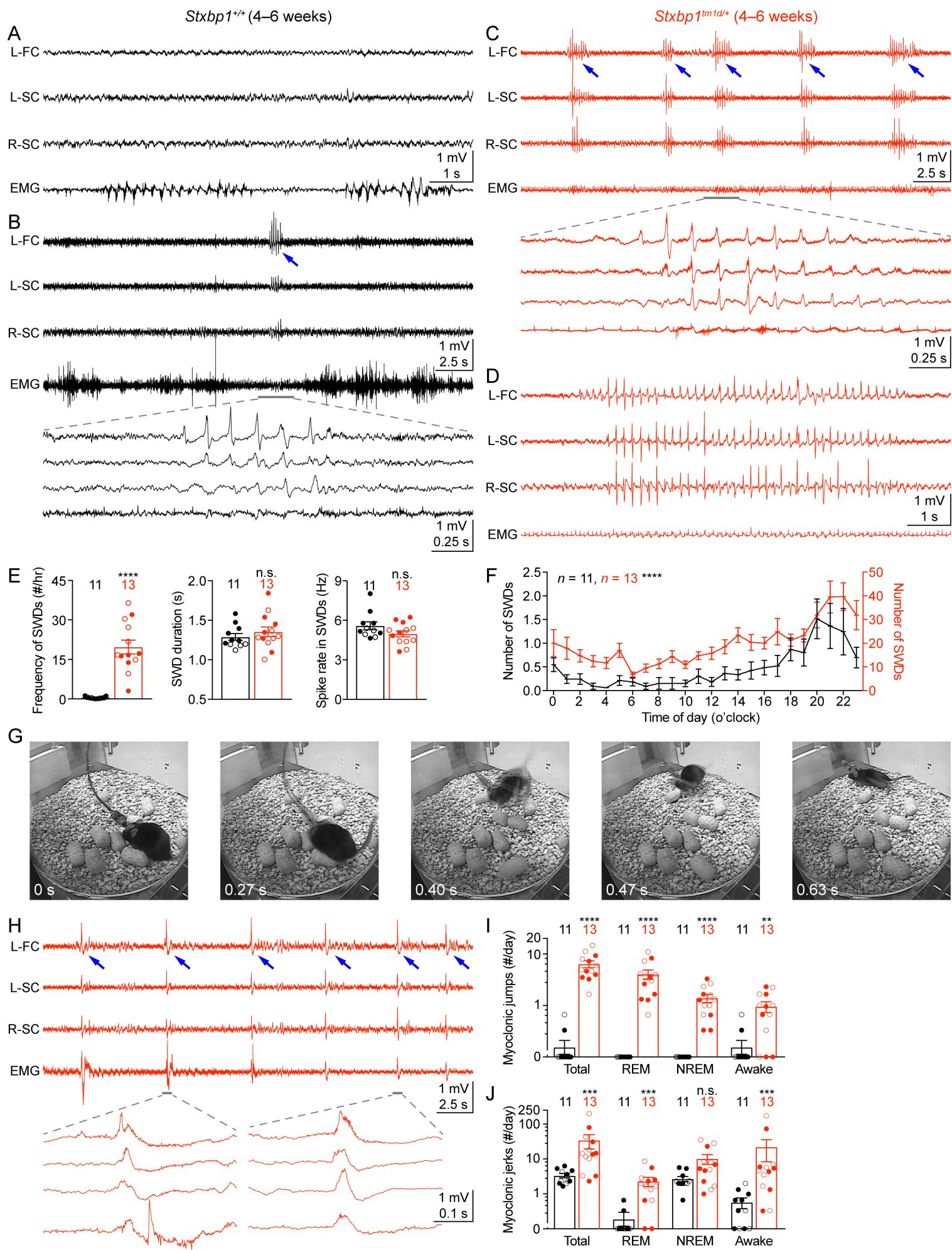


Figure 6-supplement 1

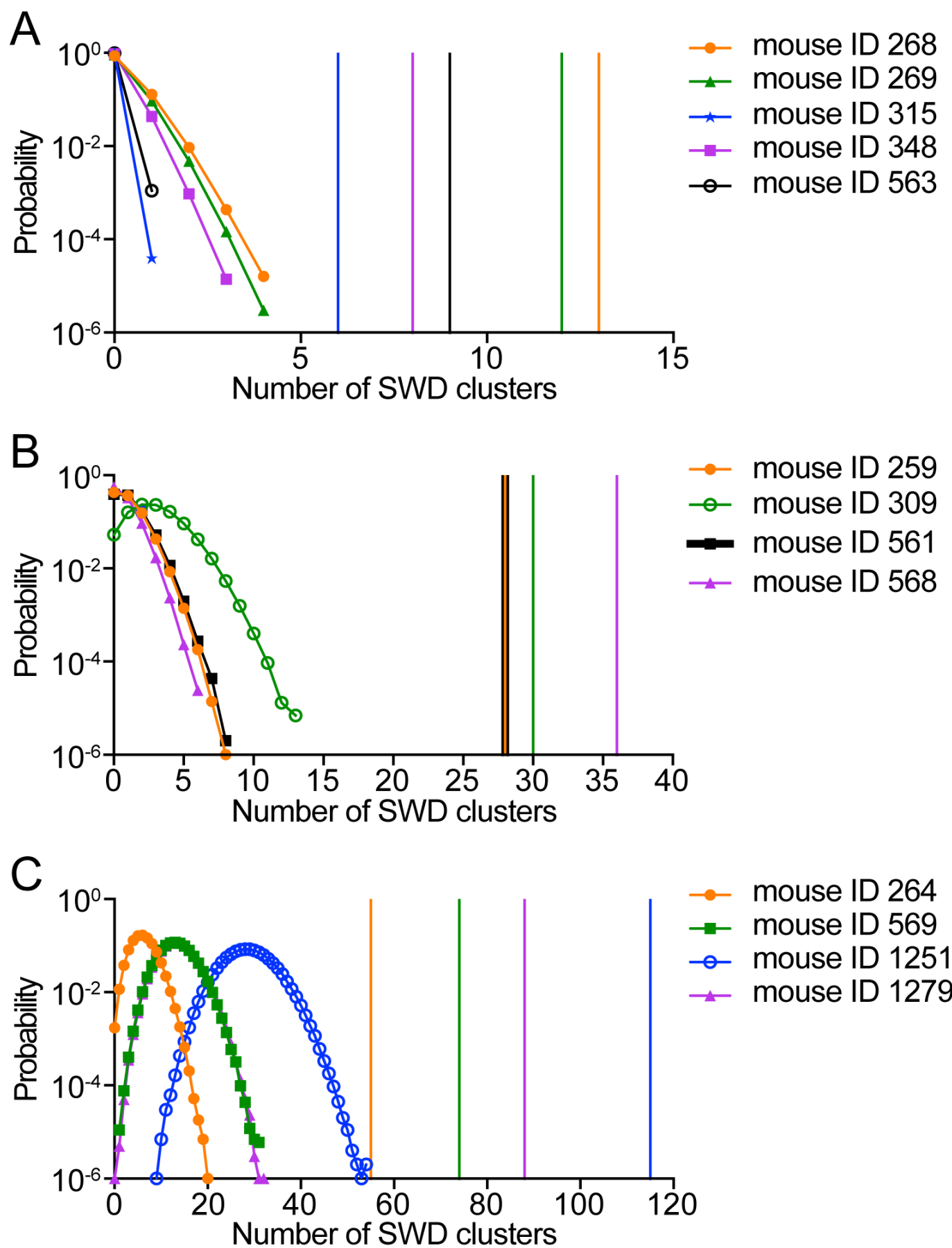
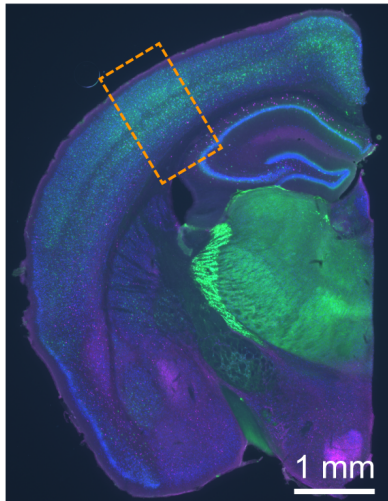
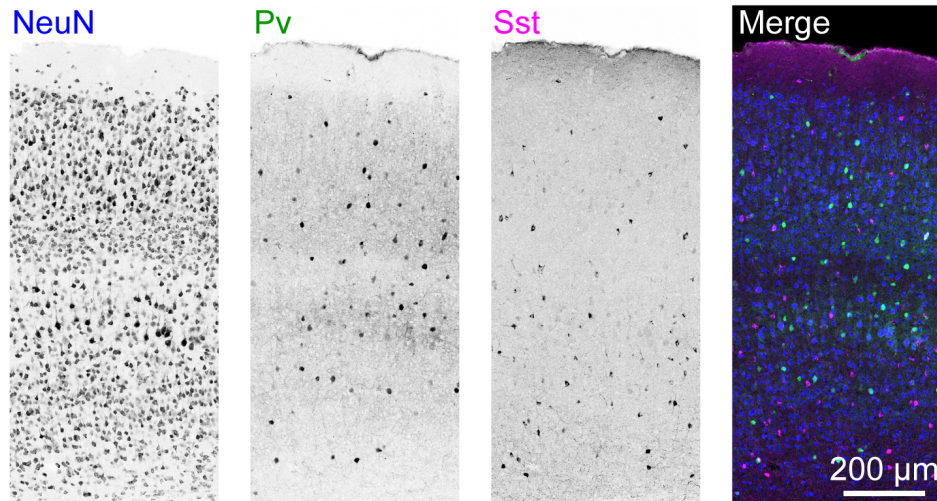


Figure 7

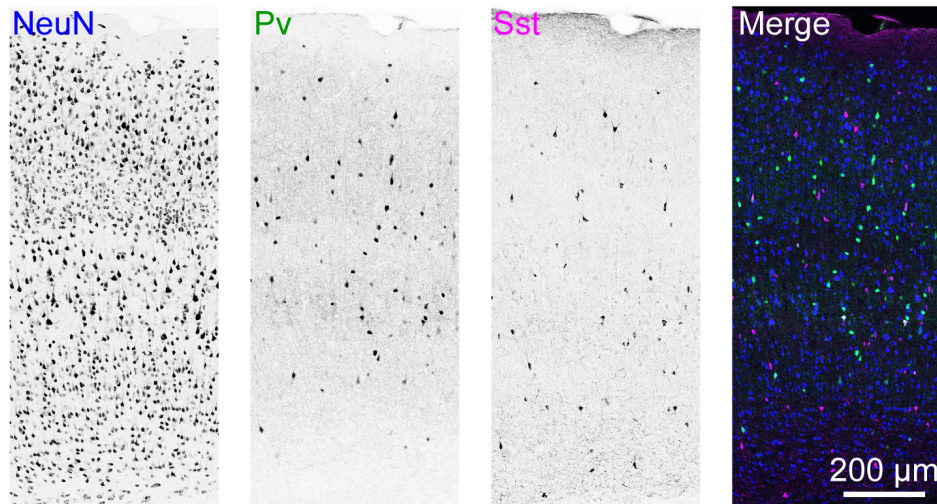
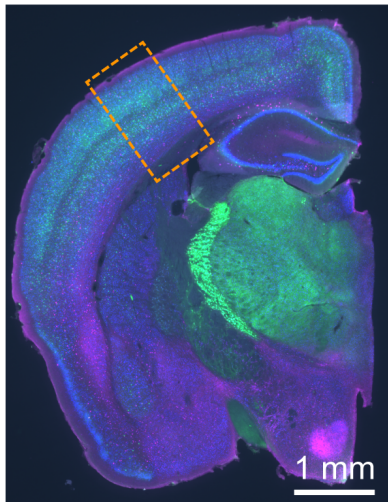
A *Stxbp1*^{+/+} (2–4 months)



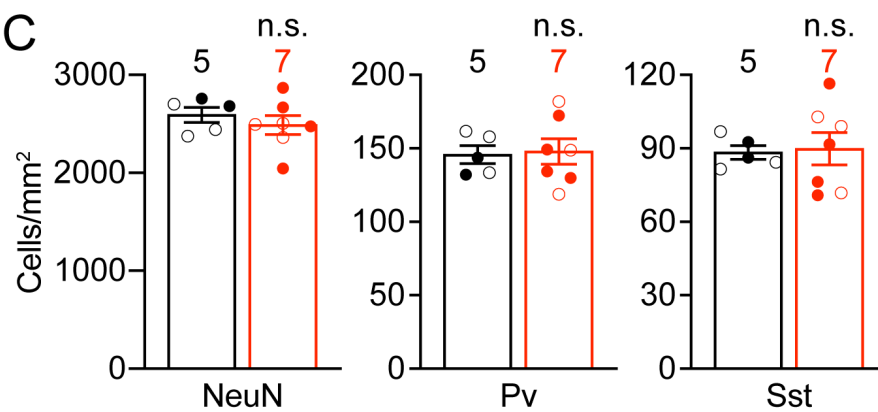
B



Stxbp1^{tm1d/+} (2–4 months)



C



D

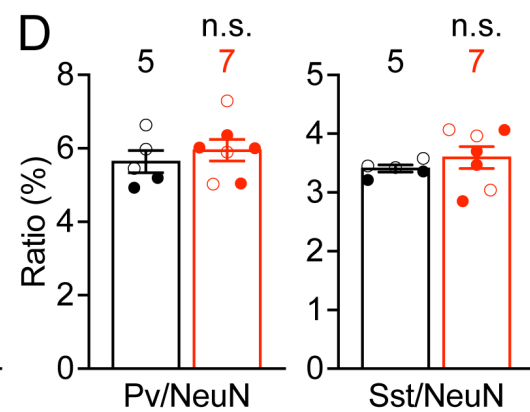


Figure 8

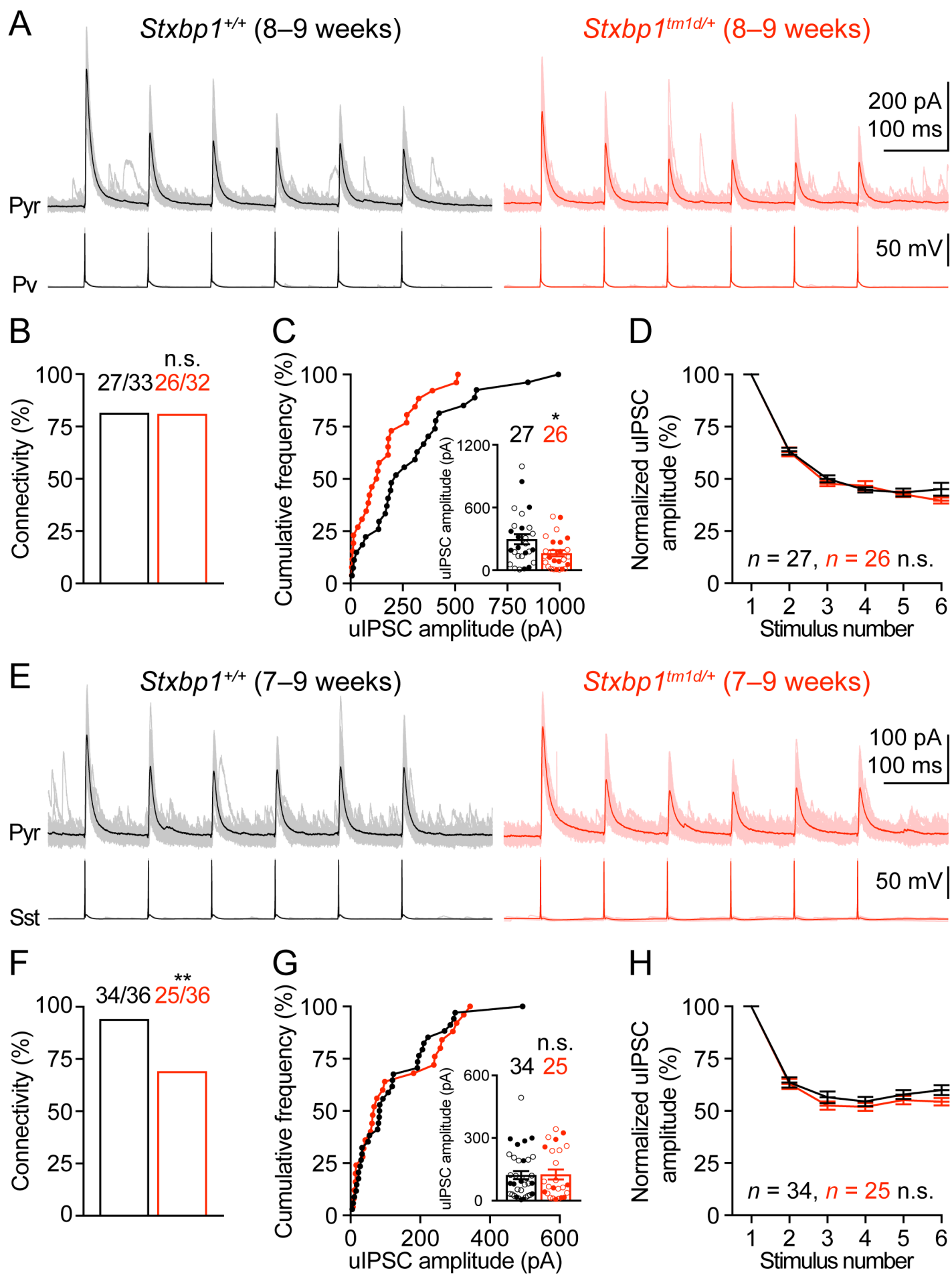


Figure 8-supplement 1

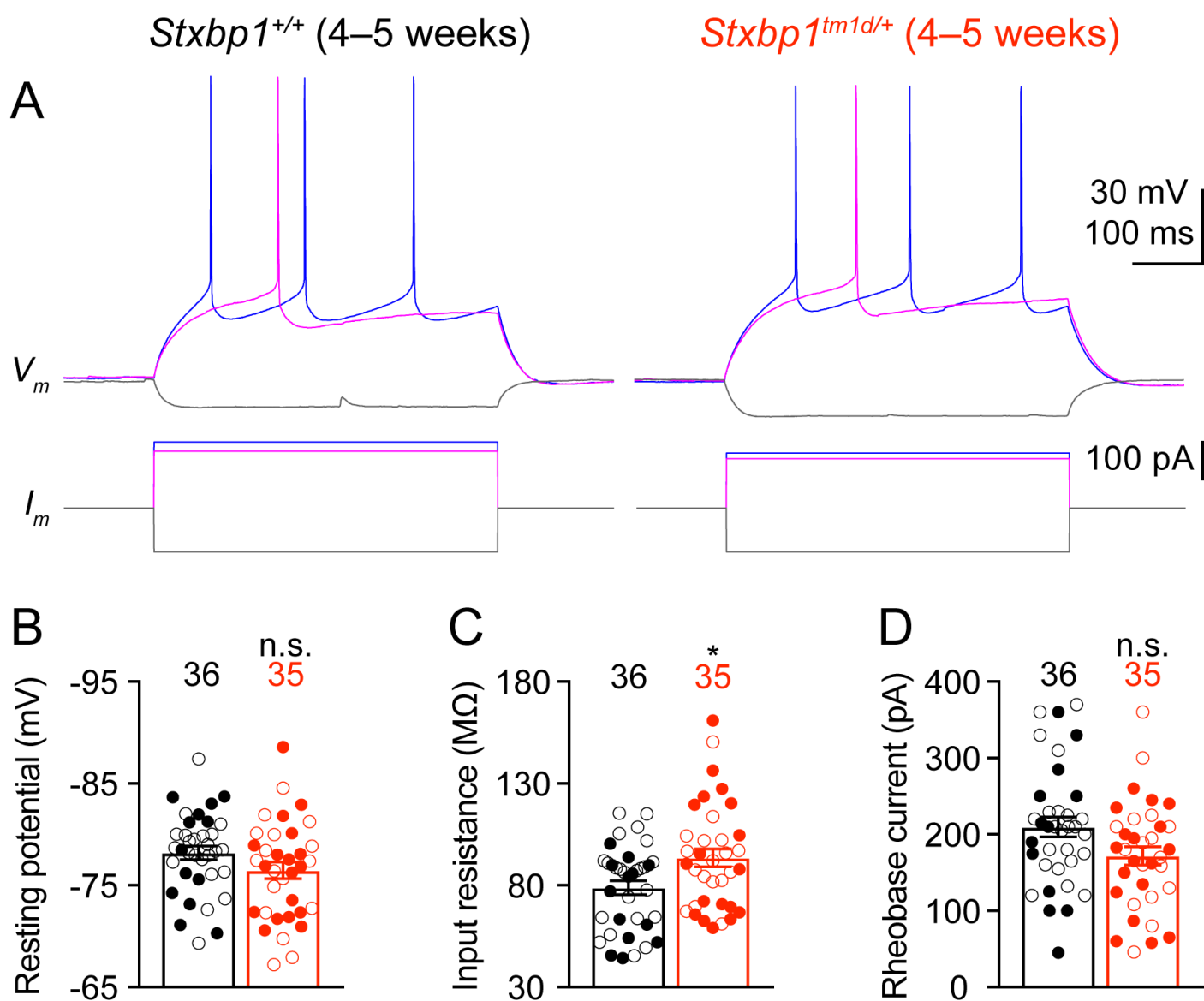


Figure 8-supplement 2

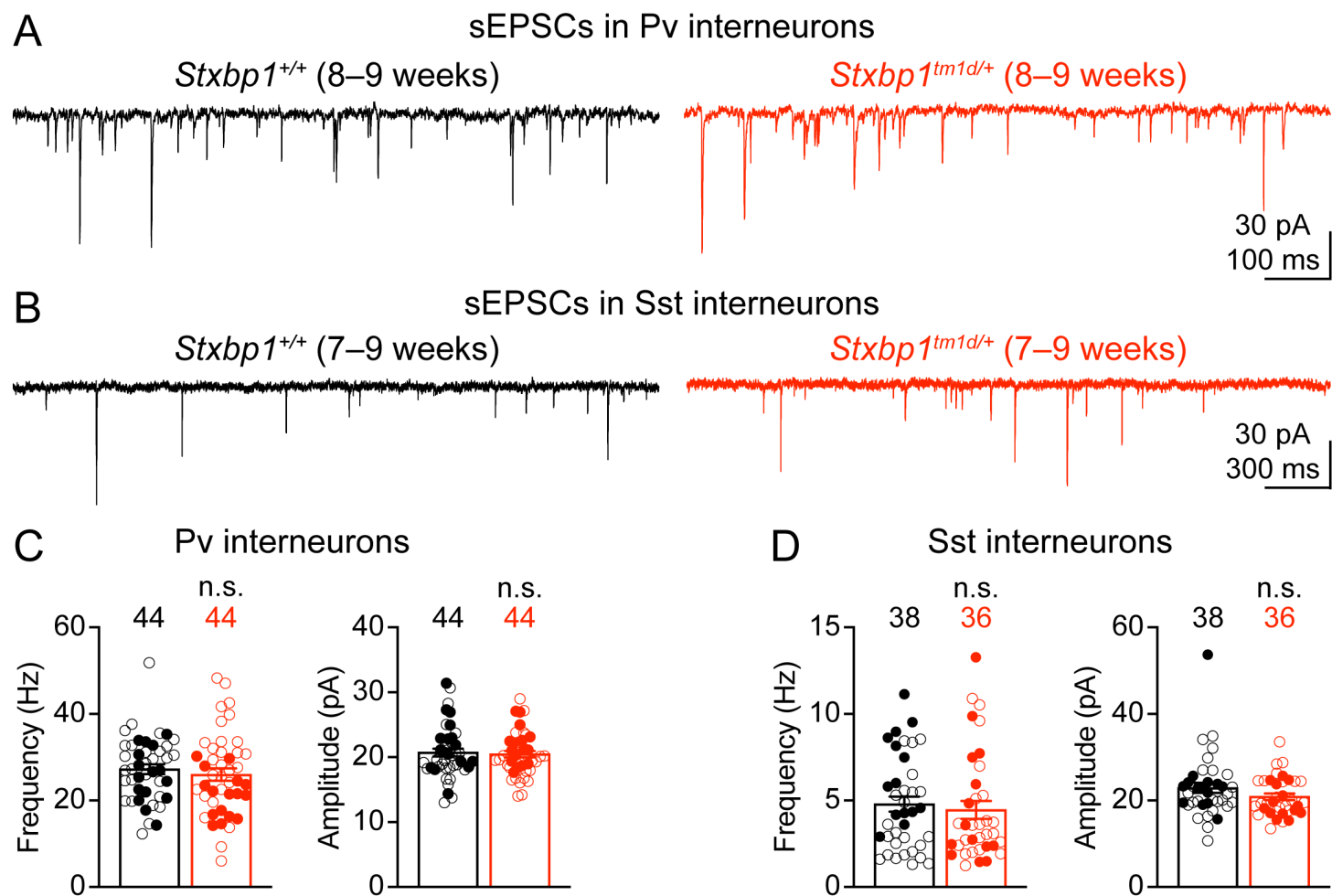


Figure 9

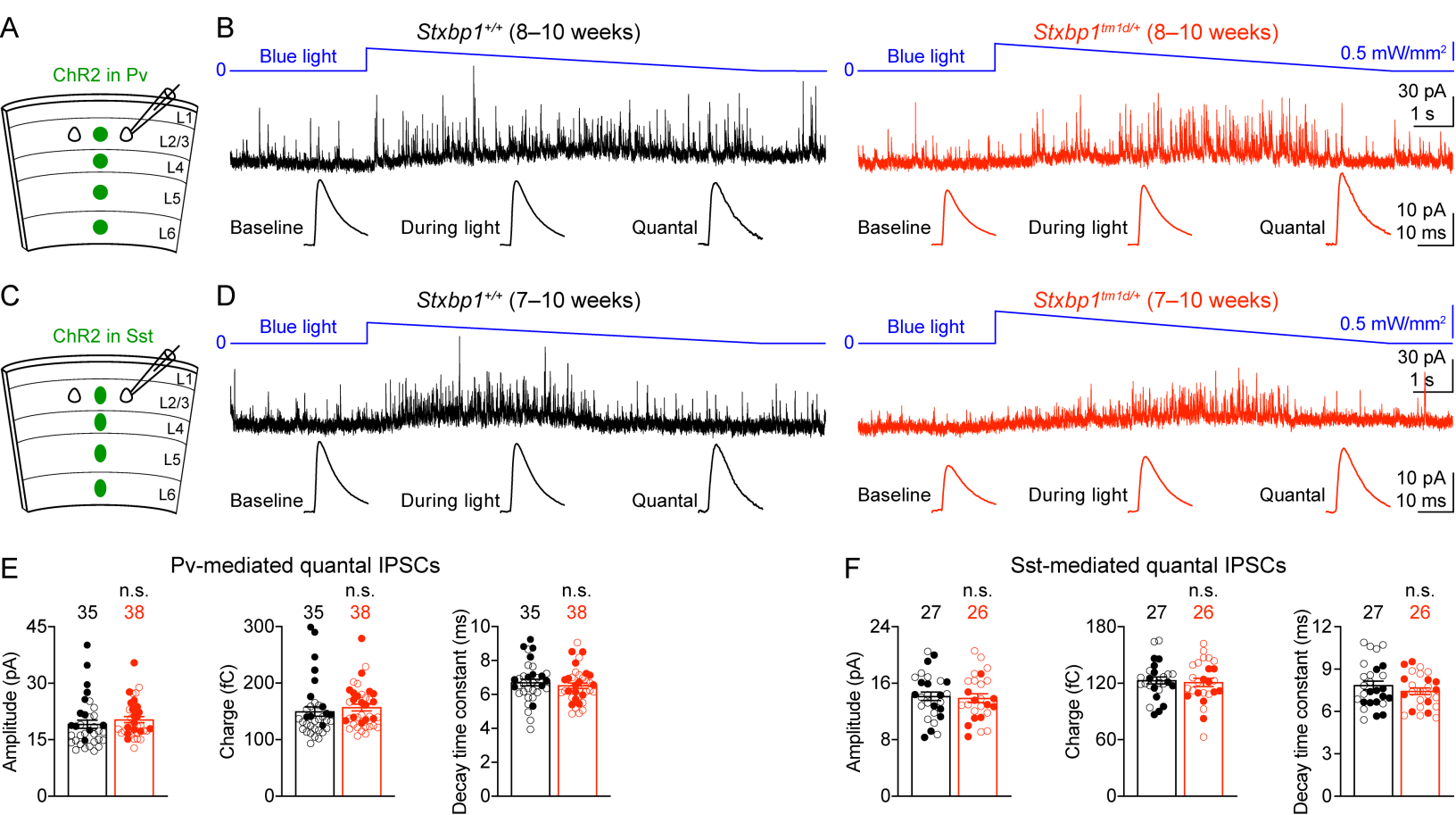


Figure 9-supplement 1

